NANO LETTERS

pubs.acs.org/NanoLett Letter

Hot-Carrier Transfer across a Nanoparticle–Molecule Junction: The Importance of Orbital Hybridization and Level Alignment

Jakub Fojt, Tuomas P. Rossi, Mikael Kuisma, and Paul Erhart*

Cite This: https://doi.org/10.1021/acs.nanolett.2c02327 Read Online

ACCESS | Metrics & More | Article Recommendations | Supporting Information

ABSTRACT: While direct hot-carrier transfer can increase photocatalytic activity, it is difficult to discern experimentally and competes with several other mechanisms. To shed light on these aspects, here, we model from first-principles hot-carrier generation across the interface between plasmonic nanoparticles and a CO molecule. The hot-electron transfer probability depends non-monotonically on the nanoparticle–molecule distance and can be effective at long distances, even before a strong chemical bond can form; hot-hole transfer on the other hand is limited to shorter distances. These observations can be explained by the energetic alignment between molecular and nanoparticle states as well as the excitation frequency. The hybridization of the molecular orbitals is the key predictor for hot-carrier transfer in these systems, emphasizing the necessity of ground state hybridization for accurate predictions. Finally, we show a nontrivial dependence of the hot-carrier distribution on the excitation energy, which could be exploited when optimizing photocatalytic systems.

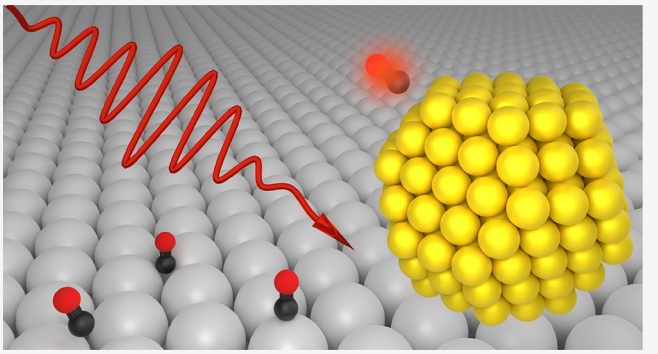

KEYWORDS: *Hot-carrier, TDDFT, Plasmonic catalysis, Nanoparticles, Adsorption*

Plasmonic metal nanoparticles (NPs) are fundamental components in several emerging technologies, including sensing,[1,2] light-harvesting,[3] solar-to-chemical energy conversion,[4−6] and catalysis.[7−10] The properties that set these materials apart for these applications are their high surface-to-volume ratios and high optical absorption cross sections at visible frequencies,[11,12] the latter being due to the presence of a localized surface plasmon (LSP) resonance.[13] In particular plasmonically driven catalysis is an active research field, addressing important chemical reactions such as ethylene epoxidation, CO oxidation, or NH_3 oxidation that are catalyzed by illuminating NPs, e.g., of the noble metals Ag,[10,14] Au,[5,6,15] or Cu.[8,9]

The LSP, which is a collective electronic excitation, is excited by absorption of light and decays within tens of femtoseconds[4,16−19,19−22] into a highly nonthermal (usually referred to as "hot") distribution of electrons and holes.[23−29] Chemical reactions can then be catalyzed by hot carriers (HCs) transiently populating orbitals of nearby molecules,[4,30] which can lower reaction barriers.[18] Two variants of this process can be distinguished. In the *direct* HC transfer process[31] (also known as chemical interface damping) the LSP decays into an electron–hole pair, where one of the carriers is localized on the reactant molecule and the other on the NP. In the *indirect* HC transfer process both carriers are generated in the NP and at a later time scattered into molecular orbitals. The efficiency and importance of these processes as well as their competition with thermal effects are still a matter of intense debate.[18,32−35] The direct HC transfer process is promising in terms of efficiency and selectivity[14,30] and has been studied experimentally,[36] in theory,[31] and by computational *ab initio* models.[20,21,37] Typically the focus lies in understanding HC generation at surfaces,[36,38] but there has not yet been a detailed account of the dependence of HC transfer on molecular position and orientation and whether there are handles for tuning HC devices to particular molecules in all probable states of thermal motion. Yet these aspects are crucial for direct HC transfer processes, which exhibit an intricate dependence on the hybridization of molecular and surface states as also shown in this work.

In this work, we study plasmon decay and carrier generation across a NP–molecule junction, which is the initial step in the direct HC transfer process. We consider plasmonic Ag, Au, and Cu NPs in combination with a CO molecule, the excitations of which are energetically much higher than the plasmon resonance of any of the NPs considered here. In a real-time time-dependent density functional theory (RT-TDDFT)[39] framework, we drive the system with an ultrafast laser pulse

Received: June 10, 2022
Revised: October 3, 2022

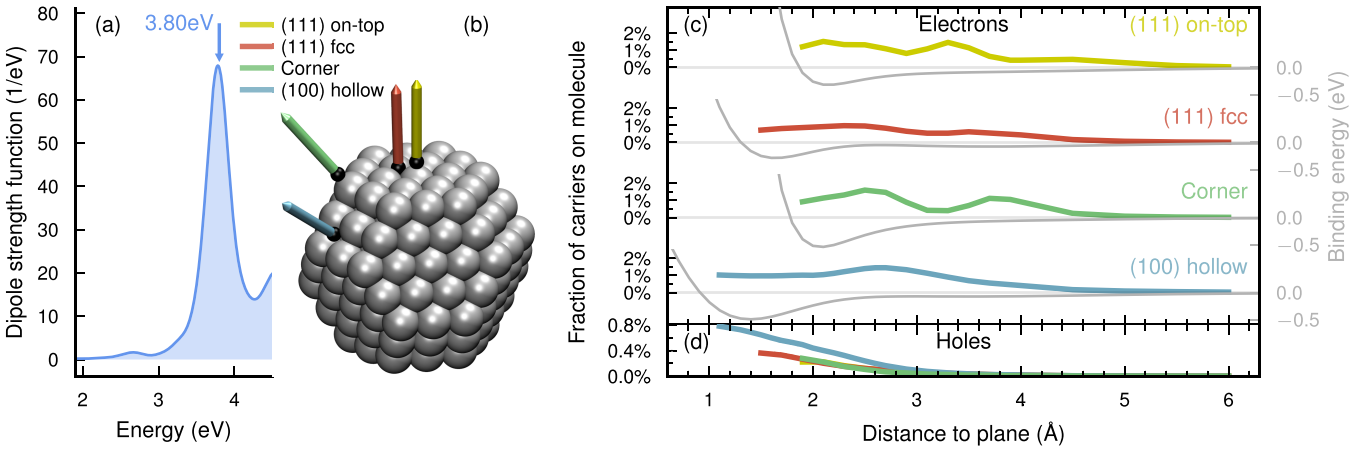

Figure 1. Geometry dependence of HC generation in Ag_{201} NP + CO. (a) Optical spectrum of the bare NP. The frequency 3.8 eV of the driving laser is marked by an arrow above the spectrum. (b) Model of the NP with the axes along which the NP−molecule distance is varied. (c, d) Fractions of generated electrons (c) and holes (d) on the molecule (eq S20) averaged in the span 25−30 fs and binding energies (eq S1) as a function of distance and site.

to induce a plasmon. We simulate the electron dynamics in the system until the plasmon has decayed and then analyze the distribution of carriers over the ground state Kohn−Sham (KS) states. To this end, we employ and extend our analysis methods,[19−21] mapping out the HC transfer efficiency as a function of the NP−molecule geometry (adsorption site, distance, molecular bond length), excitation energy, and material (Ag, Au, Cu).

We consider the CO molecule in the energetically relevant (111) on-top, (111) face-centered cubic (fcc), (100) hollow and corner sites at a range of distances from the Ag_{201} NP, which has an effective diameter of 15 Å (Supplementary Note S1[40−43]). The plasmon (3.8 eV, Figure 1a) and first optical excitation of CO (14.5 eV, Figure S1) are not resonant, and the optical response of the combined NP+CO system is not strongly dependent on geometry (Figure S2).

We drive the Ag NP + CO system with a Gaussian laser pulse with frequency $\hbar\omega$ = 3.8 eV. Within the first tens of femtoseconds a plasmon forms in the NP and decays into resonant excitations, for which the electron−hole energy difference equals $\hbar\omega$. The plasmon formation and decay process in similar systems have previously been studied in detail by our group[17,19] and are not covered here.

Varying the NP−CO distance (Figure 1b), we measure the fraction of generated electrons in the molecule after plasmon decay (Figure 1c). Interestingly while the total number of carriers is stabilized already after about 20 fs, for some configurations the fraction of generated electrons in the molecule can exhibit an oscillatory component (Figure S3). This time dependence is deserving of more detailed future studies. Here, we show the average value between 25 and 30 fs which is motivated by the fact that the plasmon has already decayed as the total number of hot carriers has reached a steady value (Figure S3).

While one could expect the fraction of hot electrons on the molecule to decrease monotonically with decreasing wave function overlap at increasing distances, we find this quantity to vary nonmonotonically between 0.5 and 2% over a wide range of distances with several site-specific features. A smooth decay to zero only occurs beyond 4−5 Å. Below this threshold several of the sites feature one or two peaks, including near 2.1 Å and 3.3 Å for the (111) on-top site, 2.7 Å for the (100) hollow site, and 2.7 Å and 3.9 Å for the corner site. Only the (111) fcc site appears relatively featureless.

By contrast, the binding energies depend smoothly on distance and approach zero already at 3−4 Å. The landscape of electron generation on the molecule thus extends further than the features in the potential energy surface and is more sensitive to the underlying shifts in eigenenergies and wave function overlaps. Our findings imply that across-interface HC generation can be effective even at quite long distances (up to 5 Å) from the NP and does not require molecular adsorption.

The fraction of holes generated on the molecule (eq S19), on the other hand, decays smoothly with distance (Figure 1d) reaching a maximum of 0.2−0.8%.

The molecular projected density of states (PDOS) (Figure 2a,d) is a key factor in explaining the rich distance dependence of the across-interface electron generation (Figure 2c,f). The energetic distribution of electrons generated on the molecule (eq S22, Figure 2b,e) clearly mirrors the shape of the molecular PDOS: a single lowest unoccupied molecular orbital (LUMO) level at 2.8 eV at long distances, shifting to lower energies with decreasing distance, eventually splitting into several branches. The mirrored shape is a necessity, as electrons are generated in the unoccupied molecular levels (i.e., where the molecular PDOS is finite); however, two additional factors determine the intensity of the branches. As the transitions ($\varepsilon_i \rightarrow \varepsilon_a$) induced by the plasmon decay are resonant with the pulse frequency ($\varepsilon_a - \varepsilon_i = \hbar\omega_{pulse}$ = 3.8 eV), the NP PDOS must align with the molecular PDOS by a constant shift of $\hbar\omega_{pulse}$ (Figure 2, inset). Finally, the strength of the coupling of each electron and hole (via the plasmon decay) is specific to the pair of states (Figure S4). Summarizing the recipe for high across-interface electron generation of energy ε, (1) the molecular PDOS must be large at ε, (2) the NP PDOS must be large at $\varepsilon - \hbar\omega$, and (3) the transition dipole moment between the corresponding NP and molecular states must be sizable.

The energetic level alignment is a good descriptor for predicting across-interface HC generation, while surface HC distributions in bare NPs are insufficient for the direct transfer pathway (Supplementary Note S2). PDOSs are usually much simpler to obtain than the transition matrix elements, and we may assess the basic possibility for HC transfer already using

https://doi.org/10.1021/acs.nanolett.2c02327
Nano Lett. XXXX, XXX, XXX−XXX

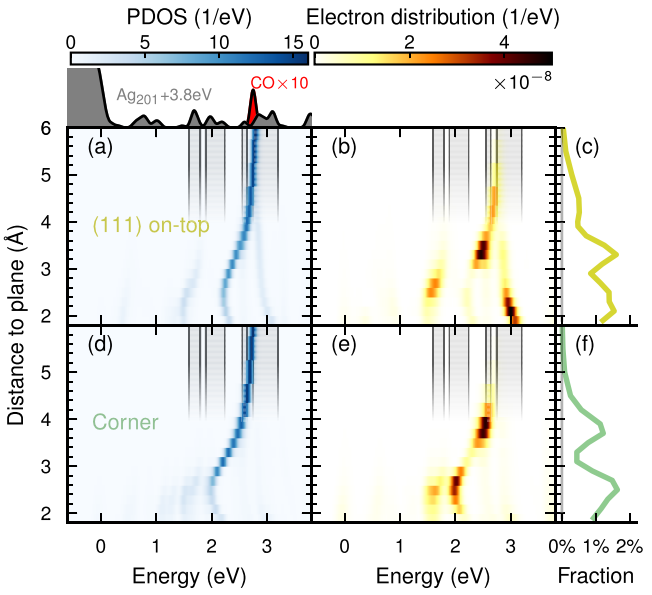

Figure 2. Level alignment between molecular and NP PDOS for (111) on-top (a–c) and corner (d–f) sites. (a, d) Molecular PDOS as a function of distance. The NP PDOS is distance-independent due to the large size of the NP. As the molecule approaches the NP, the LUMO shifts to lower energies, eventually splitting into several branches. The PDOS for the NP and molecule at far separation are indicated above the plot, where the NP PDOS has been shifted by the pulse frequency. Shaded regions correspond to (a selection of) large values in the shifted NP PDOS. (b, e) Electron distribution as a function of distance. (c, f) The fraction of electrons generated in the molecule.

the former. The latter (being affected by factors such as wave function overlap and the orbital momentum character of states) is unnecessary for a qualitative description.

Due to the finite line width of the excitation pulse (here the half-width at half-maximum is 0.37 eV), alignment does not have to be exact. In fact, scrutinizing the decomposition of the electrons distribution in terms of the underlying single-particle excitations (Figure S4) shows that the states with the strongest coupling are slightly misaligned with respect to $\hbar\omega_{\text{pulse}}$. In the following, we will find that a slight reduction in the excitation frequency leads to a notable increase in the HC transfer probability, as this improves the alignment.

In a similar manner to that of electrons, we can understand the across-interface generation of holes, with the rule that an occupied state ε in the molecule must align with a peak in the NP PDOS at $\varepsilon + \hbar\omega$. As the CO highest occupied molecular orbital (HOMO) level is at −4.8 eV in the free molecule (long distance limit), hole generation is not possible with the pulse frequency 3.8 eV. Transfer is only possible at close distances where hybridized branches of the HOMO and LUMO appear in the region $-3.8\ \text{eV} < \varepsilon < 0\ \text{eV}$, beginning at distances around 2.5 Å (Figure S5).

We now extend our study to also include Au and Cu. The s-electrons have nearly identical densities of state (DOSs) in the Ag_{201}, Au_{201}, and Cu_{201} NPs but the d-band onsets differ (Ag, 3.7 eV; Au, 2.1 eV; Cu, 2.3 eV below the Fermi level; Figure S6). As a consequence of the earlier d-band onset, Au_{201} and Cu_{201} lack the well-defined LSP peak of Ag_{201}[44] (Figure 3a). The binding energy curves are also similar to Ag, with the main difference that the molecule binds more strongly and closer to Cu (Figure S7).

We drive the NP + CO with a Gaussian laser pulse (Ag, frequency 3.8 eV; Au, 2.5 eV; Cu, 2.7 eV) and measure the fraction of electrons generated on the molecule (Figure 3b–e). We observe similar trends in Ag and Cu, both exhibiting peaks near 2.1 Å for the (111) on-top site, 2.7 Å for the (100) hollow site, and 2.7 Å and 3.9 Å for the corner site. Only the 3.3 Å peak in the (111) on-top site of Ag lacks a counterpart in Cu. In contrast to Ag and Cu, the Au NP shows smooth trends, without pronounced peaks, of decreasing electron generation on the molecule with increasing distance.

The similarity in electron generation for Ag and Cu can be explained by a similar distance dependence of the molecular orbital hybridization (Figure S5). While the resonance condition is not the same for Ag and Cu ($\hbar\omega$ = 3.8 and 2.7 eV, respectively), the similar energy-spacing between hybridized molecular levels is enough to yield similar electron generation curves. The 3.3 Å peak is the only clear feature that is missing in Cu, the reason being that the molecular orbital is too far from the Fermi level (2.8 eV, to be compared to $\hbar\omega$ = 2.7 eV). The hybridization behavior in Au differs from the behavior in Ag and Cu. At long distances the CO LUMO is

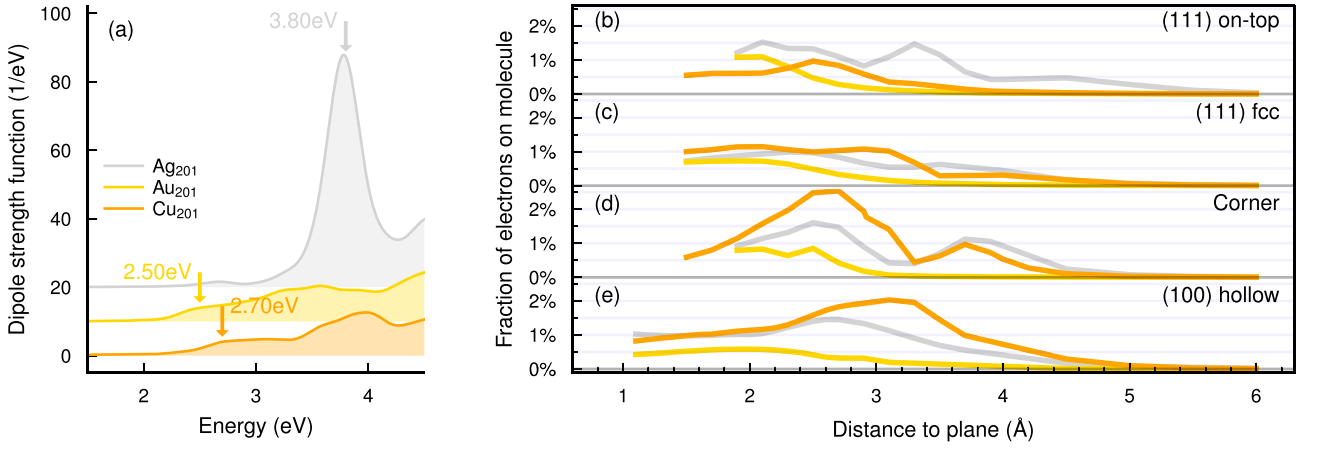

Figure 3. Geometry dependence of electron generation in Ag_{201}, Au_{201}, and Cu_{201} NPs + CO. (a) Optical spectra of the bare NPs. (b–e) Fractions of generated electrons on the molecule (eq S20) after plasmon decay as a function of distance and site with pulse frequency 3.8 eV (Ag), 2.5 eV (Au), and 2.7 eV (Cu).

https://doi.org/10.1021/acs.nanolett.2c02327
Nano Lett. XXXX, XXX, XXX−XXX

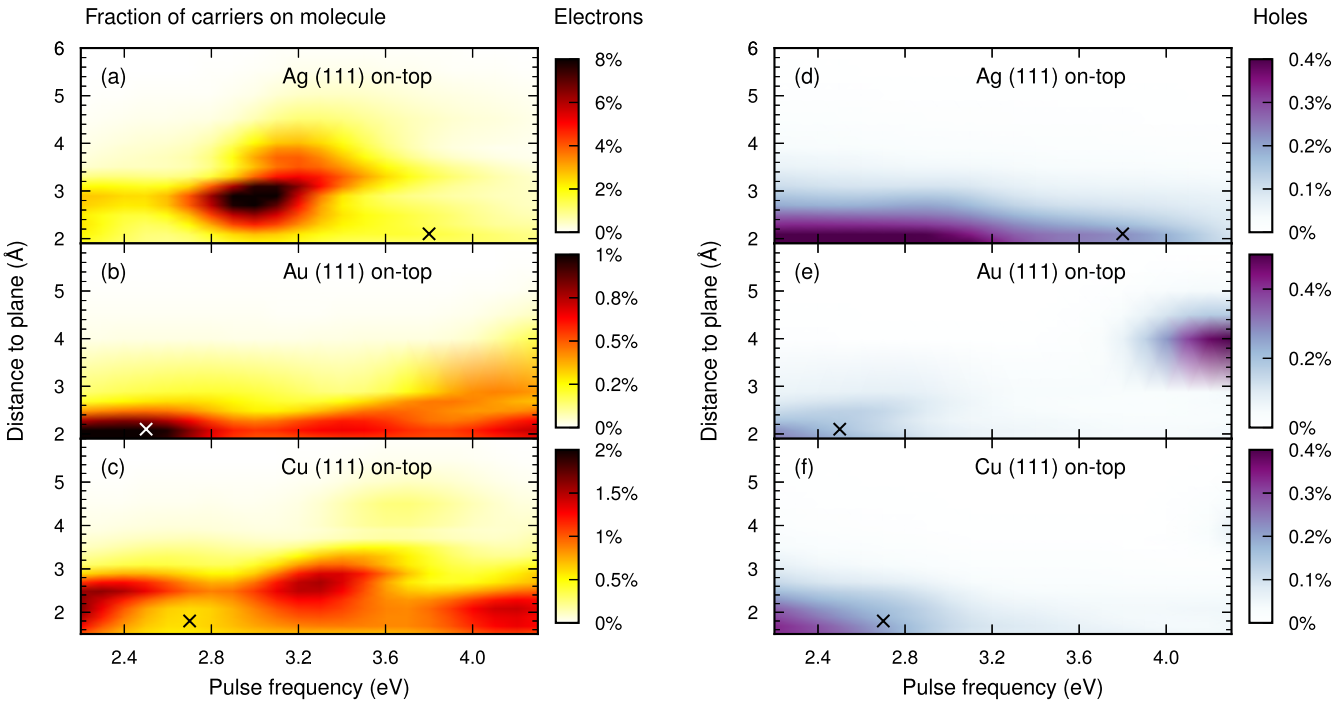

Figure 4. Pulse-frequency dependence of the electron generation in CO. Fraction of generated electrons (a–c) and holes (d–f) on the molecule as a function of distance and pulse frequency for the (111) on-top site in Ag (a, d), Au (b, e), and Cu (c, f). For reference, the crosses in the figure mark the distance corresponding to the adsorption minimum, and the pulse frequency used in Figure 3.

further from the Fermi level in Au than in Ag or Cu (due to Au having a higher work function and us considering different bond length of the molecule for each metal), preventing electron generation. As the distance decreases, the orbital hybridizes more strongly, splitting into more branches. As a consequence, at small distances there are more PDOS branches in which electron generation occurs, leading to a smoother distance dependence.

Based on our observations, we should expect the pulse frequency $\hbar\omega$ to act as a handle for tuning the electron generation through the approximate (barring electron–hole coupling) resonance condition $\varepsilon_a - \varepsilon_i = \hbar\omega$. Indeed, the electron generation depends nonmonotonically on both distance and pulse frequency (Figure 4a–c). For example, by lowering the pulse frequency we can avoid the dip in electron generation at 2.9 Å for the Ag (111) on-top site; using $\hbar\omega$ = 3.1 eV, the feature at the same distance instead becomes a maximum. Choosing the pulse frequency appropriately, the fraction of electrons generated on the molecule can be as high as 8.9% for Ag (distance 2.7 Å, $\hbar\omega$ = 3.1 eV), 1.1% for Au (distance 1.9 Å, $\hbar\omega$ = 2.2 eV), and 2.3% for Cu (distance 2.1 Å, $\hbar\omega$ = 2.2 eV). While the electron generation in the Ag and Cu systems shows a complex dependence on pulse frequency and distance, in the case of Au, it is almost monotonic in both dimensions. However, in both end points of the considered pulse frequencies the behavior for Au becomes more interesting; at low frequencies the distance dependence becomes very sharp, as fewer PDOS branches fall into the relevant energy range, and at high frequencies there is electron generation at long distances, due to the free-molecule LUMO falling into the relevant energy range.

In the case of Ag (Figure 4d) and Cu (Figure 4f), holes are generated at small distances (where hybridized branches of the LUMO orbital are below the Fermi energy; Figure S5) with a weak dependence on pulse frequency. For Au (Figure 4e) hole generation becomes relatively strong at intermediate distances (3–5 Å) and large pulse frequencies. This behavior originates from the HOMO orbital, which in the long-distance limit resides 3.9 eV below the Fermi energy but shifts to lower energies with decreasing distance (i.e., out of the range $\varepsilon_a - \varepsilon_i = \hbar\omega$, $\varepsilon_a > 0$, thus limiting hole generation).

The frequency of the exciting light is thus an excellent handle for tuning the fraction of carriers generated on the molecule, which is especially interesting in applications where selectivity is important. In molecules with several orbitals close enough to the Fermi energy to be optically accessible, the generation of electrons in one orbital could be favored over the other. It is, however, important at this stage to remember that changing the pulse frequency also changes the total optical absorption and thus the total number of generated carriers. We therefore also consider the total, pulse-frequency and distance-dependent, amount of electrons generated on the molecule (Figure S8, that is, contrary to before, *without* expressing it as a fraction of electrons generated in the entire NP + CO system). In particular for the Ag NP, which has a very sharp absorption spectrum, the pulse dependence is affected, with a maximum in total electron generation on the molecule occurring using a pulse frequency of 3.6 eV (to be compared to a maximum in the fraction of electrons generated on the molecule at 3.1 eV). As a final note, we point out that it should be possible to simultaneously tune the pulse frequency to the desired resonance condition $\varepsilon_a - \varepsilon_i = \hbar\omega$, and the LSP resonance of the NP (thus the optical absorption) to the pulse frequency, by taking advantage of the fact that the LSP is more sensitive to the size and shape of the NP than, for example, the DOS.

In this study we have investigated the geometry dependence of HC generation across noble metal–molecule interfaces due to plasmon absorption and decay. We have found that typically up to 0.5–3% of all electrons generated in the system end up on the molecule after plasmon decay, even up to distances of 5

https://doi.org/10.1021/acs.nanolett.2c02327
Nano Lett. XXXX, XXX, XXX–XXX

Å, which is well before a strong chemical bond can form. By tuning the excitation frequency, we are able to achieve up to 8.9% electrons generated in the molecule, at the expense of a lower absolute amount of electrons generated. These findings suggest that direct HC transfer is a relevant process in plasmon decay and that the process does not require the formation of a strong chemical bond between the molecule and the absorbing medium.

We have also shown that the fraction of generated electrons on the molecule depends on the geometry of the molecule and NP in rather intricate fashion. This geometry dependence can be understood in terms of the energy landscape of hybridized molecular orbitals; as an orbital shifts so it is resonant with certain peaks in the NP PDOS, an increase in the probability for HC transfer can be expected. The distance-dependent behavior of the hybridization differs enough for the various sites so that the carrier generation also differs. For larger NPs, where the DOS between d-band onset and Fermi level is more smeared out, these effects could be less important.

In HC transfer processes the rate of charge carrier generation across the metal−molecule interface is in competition with various loss channels, such as the rates of reemission and scattering and subsequent thermalization of excited carriers with phonons, surfaces, and other carriers.[16,26] The most important mechanisms in this context are electron−electron and (to a lesser degree) electron−phonon scattering, which are necessary for the HC distribution to thermalize to a Fermi−Dirac distribution. As these loss channels are currently beyond the reach of our calculations, we can view our results as an upper bound on the efficiency of HC transfer, i.e., out of all photon absorption events that occur, up to 0.5−3% (or 8.9% when tuning the excitation frequency) result in electron transfer to the molecule. It is worthwhile to point out that HC generation is a quantized process, where it is very unlikely that there is at one time more than one excited plasmon at a time, under illumination conditions that are realistic for energy-harvesting applications.[26,27] Each plasmon decays into one electron−hole pair where one carrier can be either in the molecule or in the metal, and we should thus consider our computed fractions as probabilities. We also emphasize that the numbers we report are specific for the NP size and adsorbate coverage considered here.

For the purpose of a quantitative comparison to experimental realizations, it is crucial to consider that while metal states are accurately described with our level of theory,[45] molecular states are not. We should thus expect transfer maxima to occur for different geometrical configurations, due to slightly shifted (hybridized) molecular orbitals; however, our general conclusions are still valid.

The importance of ground state hybridization for HC transfer implies that theoretical modeling should not be restricted to considering bare metal surfaces, without taking interactions with molecules into account. The distance-dependent hybridization of molecular orbitals should be explicitly taken into account for meaningful predictions. Our results suggest that since already the ground state of the hybridized system is a good descriptor for prediction of HC generation on molecules, rapid screening of candidates of good systems can be performed without conducting expensive real-time simulations.

We close by commenting on the possibilities for tuning HC transfer suggested by the results of this study. HC devices can be designed by tuning the resonance condition to achieve a desired purpose; handles for tuning to a certain molecular orbital are the NP DOS, surface substitutions that affect the hybridization of the orbital, and the frequency of the incoming light. As we have demonstrated, the tuning of the last influences the absorption cross section so that there is a trade-off between high fraction of carriers transferred and high amount of carriers generated in total. It is possible, however, to shift the absorption maximum with a rather small impact on level alignment by modifying the NP shape and size so that there is a maximum in both absorption and transfer. In this way one ought to be able to maximize HC transfer. Furthermore, the sharp LSP resonances of Ag NPs could possibly be utilized in the design of highly selective catalysts that work with broadband (solar) light; if the NP PDOS consists of one particularly strong peak and that peak is resonant with one specific molecular orbital with the frequency of the LSP resonance, then transfer to that specific orbital will be preferred over transfer to other orbitals.

SOFTWARE USED

The VASP[46−49] suite with the projector augmented wave (PAW)[50] method and the vdW-df-cx[51−54] exchange correlation (XC) functional was used for the total energy calculations and structure relaxations. The GPAW package[55,56] with linear combination of atomic orbitals (LCAO) basis sets[57] and the LCAO-RT-TDDFT implementation[58] was used for the RT-TDDFT calculations. The Gritsenko−van Leeuwen−van Lenthe−Baerends solid correlation (GLLB-sc)[45,59] XC-functional, utilizing the Libxc[60] library, was used in GPAW. The ASE library[61] was used for constructing and manipulating atomic structures. The NumPy,[62] SciPy,[63] and Matplotlib[64] Python packages and the VMD software[65,66] were used for processing and plotting data. The Snakemake[67] package was used for managing the calculation workflow.

ASSOCIATED CONTENT

Supporting Information

The Supporting Information is available free of charge at https://pubs.acs.org/doi/10.1021/acs.nanolett.2c02327.

Supporting data for our results in Figures S1−S15 and Supplementary Table S1; details concerning our methodology, the systems under study, and the parameters used in computations provided in Supplementary Notes S1−S4 (PDF)

AUTHOR INFORMATION

Corresponding Author

Paul Erhart − *Department of Physics, Chalmers University of Technology, SE-412 96 Gothenburg, Sweden;* orcid.org/0000-0002-2516-6061; Email: erhart@chalmers.se

Authors

Jakub Fojt − *Department of Physics, Chalmers University of Technology, SE-412 96 Gothenburg, Sweden;* orcid.org/0000-0002-8372-3153

Tuomas P. Rossi − *Department of Applied Physics, Aalto University, FI-00076 Aalto, Finland;* orcid.org/0000-0002-8713-4559

Mikael Kuisma − *Department of Physics, Technical University of Denmark, DK-2800 Kongens Lyngby, Denmark;* orcid.org/0000-0001-8323-3405

Complete contact information is available at:

https://doi.org/10.1021/acs.nanolett.2c02327
Nano Lett. XXXX, XXX, XXX−XXX

https://pubs.acs.org/10.1021/acs.nanolett.2c02327

Notes

The authors declare no competing financial interest.

Data Availability. The data generated in this study are openly available via Zenodo at https://doi.org/10.5281/zenodo.6524101.

■ ACKNOWLEDGMENTS

We gratefully acknowledge helpful discussions with Patrick Rinke. This research has been funded by the Knut and Alice Wallenberg Foundation (Grants 2015.0055 and 2019.0140; J.F. and P.E.), the Swedish Foundation for Strategic Research Materials framework (Grant RMA15-0052; J.F. and P.E.), the Swedish Research Council (Grants 2015-04153 and 2020-04935; J.F. and P.E.), the European Union's Horizon 2020 Research and Innovation Programme under the Marie Skłodowska-Curie Grant Agreement 838996 (T.P.R.), and the Academy of Finland under Grant 332429 (T.P.R.). The computations were enabled by resources provided by the Swedish National Infrastructure for Computing (SNIC) at NSC, C3SE, and PDC partially funded by the Swedish Research Council through Grant Agreement 2018-05973 as well as by the CSC—IT Center for Science, Finland, and by the Aalto Science-IT project, Aalto University School of Science.

■ REFERENCES

(1) Nugroho, F. A. A.; Darmadi, I.; Cusinato, L.; Susarrey-Arce, A.; Schreuders, H.; Bannenberg, L. J.; da Silva Fanta, A. B.; Kadkhodazadeh, S.; Wagner, J. B.; Antosiewicz, T. J.; Hellman, A.; Zhdanov, V. P.; Dam, B.; Langhammer, C. Metal−Polymer Hybrid Nanomaterials for Plasmonic Ultrafast Hydrogen Detection. *Nat. Mater.* **2019**, *18*, 489−495.

(2) Darmadi, I.; Khairunnisa, S. Z.; Tomeček, D.; Langhammer, C. Optimization of the Composition of PdAuCu Ternary Alloy Nanoparticles for Plasmonic Hydrogen Sensing. *ACS Applied Nano Materials* **2021**, *4*, 8716−8722.

(3) Geng, X.; Abdellah, M.; Bericat Vadell, R.; Folkenant, M.; Edvinsson, T.; Sa, J. Direct Plasmonic Solar Cell Efficiency Dependence on Spiro-OMeTAD Li-TFSI Content. *Nanomaterials* **2021**, *11*, 3329.

(4) Aslam, U.; Rao, V. G.; Chavez, S.; Linic, S. Catalytic Conversion of Solar to Chemical Energy on Plasmonic Metal Nanostructures. *Nature Catalysis* **2018**, *1*, 656−665.

(5) Li, R.; Cheng, W.-H.; Richter, M. H.; DuChene, J. S.; Tian, W.; Li, C.; Atwater, H. A. Unassisted Highly Selective Gas-Phase CO2 Reduction with a Plasmonic Au/p-GaN Photocatalyst Using H2O as an Electron Donor. *ACS Energy Letters* **2021**, *6*, 1849−1856.

(6) DuChene, J. S.; Tagliabue, G.; Welch, A. J.; Cheng, W.-H.; Atwater, H. A. Hot Hole Collection and Photoelectrochemical CO2 Reduction with Plasmonic Au/p-GaN Photocathodes. *Nano Lett.* **2018**, *18*, 2545−2550.

(7) Zhou, L.; Lou, M.; Bao, J. L.; Zhang, C.; Liu, J. G.; Martirez, J. M. P.; Tian, S.; Yuan, L.; Swearer, D. F.; Robatjazi, H.; Carter, E. A.; Nordlander, P.; Halas, N. J. Hot Carrier Multiplication in Plasmonic Photocatalysis. *Proc. Natl. Acad. Sci. U. S. A.* **2021**, *118*, No. e2022109118.

(8) DuChene, J. S.; Tagliabue, G.; Welch, A. J.; Li, X.; Cheng, W.-H.; Atwater, H. A. Optical Excitation of a Nanoparticle Cu/p-NiO Photocathode Improves Reaction Selectivity for CO2 Reduction in Aqueous Electrolytes. *Nano Lett.* **2020**, *20*, 2348−2358.

(9) Hou, T.; Chen, L.; Xin, Y.; Zhu, W.; Zhang, C.; Zhang, W.; Liang, S.; Wang, L. Porous CuFe for Plasmon-Assisted N2 Photofixation. *ACS Energy Letters* **2020**, *5*, 2444−2451.

(10) Yamazaki, Y.; Kuwahara, Y.; Mori, K.; Kamegawa, T.; Yamashita, H. Enhanced Catalysis of Plasmonic Silver Nanoparticles by a Combination of Macro-/Mesoporous Nanostructured Silica Support. *J. Phys. Chem. C* **2021**, *125*, 9150−9157.

(11) Bohren, C. F. How Can a Particle Absorb More than the Light Incident on It? *Am. J. Phys.* **1983**, *51*, 323−327.

(12) Langhammer, C.; Kasemo, B.; Zorić, I. Absorption and Scattering of Light by Pt, Pd, Ag, and Au Nanodisks: Absolute Cross Sections and Branching Ratios. *J. Chem. Phys.* **2007**, *126*, 194702.

(13) Kreibig, U.; Vollmer, M. *Optical Properties of Metal Clusters*; Springer Series in Materials Science 25; Springer: Berlin, 1995.

(14) Christopher, P.; Xin, H.; Linic, S. Visible-Light-Enhanced Catalytic Oxidation Reactions on Plasmonic Silver Nanostructures. *Nat. Chem.* **2011**, *3*, 467−472.

(15) Saha, S.; Yang, J.; Masouleh, S. S. M.; Botton, G. A.; Soleymani, L. Hot Hole Direct Photoelectrochemistry of Au NPs: Interband versus Intraband Hot Carriers. *Electrochim. Acta* **2022**, *404*, 139746.

(16) Bernardi, M.; Mustafa, J.; Neaton, J. B.; Louie, S. G. Theory and Computation of Hot Carriers Generated by Surface Plasmon Polaritons in Noble Metals. *Nat. Commun.* **2015**, *6*, 7044.

(17) Rossi, T. P.; Kuisma, M.; Puska, M. J.; Nieminen, R. M.; Erhart, P. Kohn−Sham Decomposition in Real-Time Time-Dependent Density-Functional Theory: An Efficient Tool for Analyzing Plasmonic Excitations. *J. Chem. Theory Comput.* **2017**, *13*, 4779−4790.

(18) Zhou, L.; Swearer, D. F.; Zhang, C.; Robatjazi, H.; Zhao, H.; Henderson, L.; Dong, L.; Christopher, P.; Carter, E. A.; Nordlander, P.; Halas, N. J. Quantifying Hot Carrier and Thermal Contributions in Plasmonic Photocatalysis. *Science* **2018**, *362*, 69−72.

(19) Rossi, T. P.; Erhart, P.; Kuisma, M. Hot-Carrier Generation in Plasmonic Nanoparticles: The Importance of Atomic Structure. *ACS Nano* **2020**, *14*, 9963−9971.

(20) Kumar, P. V.; Rossi, T. P.; Kuisma, M.; Erhart, P.; Norris, D. J. Direct Hot-Carrier Transfer in Plasmonic Catalysis. *Faraday Discuss.* **2019**, *214*, 189−197.

(21) Kumar, P. V.; Rossi, T. P.; Marti-Dafcik, D.; Reichmuth, D.; Kuisma, M.; Erhart, P.; Puska, M. J.; Norris, D. J. Plasmon-Induced Direct Hot-Carrier Transfer at Metal−Acceptor Interfaces. *ACS Nano* **2019**, *13*, 3188−3195.

(22) Villegas, C. E. P.; Leite, M. S.; Marini, A.; Rocha, A. R. Efficient Hot-Carrier Dynamics in near-Infrared Photocatalytic Metals. *Phys. Rev. B* **2022**, *105*, 165109.

(23) Brongersma, M. L.; Halas, N. J.; Nordlander, P. Plasmon-Induced Hot Carrier Science and Technology. *Nat. Nanotechnol.* **2015**, *10*, 25−34.

(24) Gong, T.; Munday, J. N. Materials for Hot Carrier Plasmonics [Invited]. *Optical Materials Express* **2015**, *5*, 2501−2512.

(25) Roman Castellanos, L.; Hess, O.; Lischner, J. Single Plasmon Hot Carrier Generation in Metallic Nanoparticles. *Commun. Phys.* **2019**, *2*, 47.

(26) Khurgin, J. B. Hot Carriers Generated by Plasmons: Where Are They Generated and Where Do They Go from There? *Faraday Discuss.* **2019**, *214*, 35−58.

(27) Khurgin, J. B. Fundamental Limits of Hot Carrier Injection from Metal in Nanoplasmonics. *Nanophotonics* **2020**, *9*, 453−471.

(28) Hattori, Y.; Meng, J.; Zheng, K.; Meier de Andrade, A.; Kullgren, J.; Broqvist, P.; Nordlander, P.; Sa, J. Phonon-Assisted Hot Carrier Generation in Plasmonic Semiconductor Systems. *Nano Lett.* **2021**, *21*, 1083−1089.

(29) Hawe, P.; Silveira, V. R. R.; Bericat Vadell, R.; Lewin, E.; Sa, J. Plasmon-Mediated Oxidation Reaction on Au/p-Cu2O: The Origin of Hot Holes. *Physchem* **2021**, *1*, 163−175.

(30) Linic, S.; Aslam, U.; Boerigter, C.; Morabito, M. Photochemical Transformations on Plasmonic Metal Nanoparticles. *Nat. Mater.* **2015**, *14*, 567−576.

(31) Khurgin, J. B.; Petrov, A.; Eich, M.; Uskov, A. V. Direct Plasmonic Excitation of the Hybridized Surface States in Metal Nanoparticles. *ACS Photonics* **2021**, *8*, 2041−2049.

(32) Dubi, Y.; Un, I. W.; Sivan, Y. Thermal Effects − an Alternative Mechanism for Plasmon-Assisted Photocatalysis. *Chemical Science* **2020**, *11*, 5017−5027.
(33) Jain, P. K. Comment on "Thermal Effects − an Alternative Mechanism for Plasmon-Assisted Photocatalysis" by Y. Dubi, I. W. Un and Y. Sivan, Chem. Sci., 2020, 11, 5017. *Chem. Sci.* **2020**, *11*, 9022−9023.
(34) Sivan, Y.; Baraban, J.; Un, I. W.; Dubi, Y. Comment on "Quantifying Hot Carrier and Thermal Contributions in Plasmonic Photocatalysis". *Science* **2019**, *364*, No. eaaw9367.
(35) Zhou, L.; Swearer, D. F.; Robatjazi, H.; Alabastri, A.; Christopher, P.; Carter, E. A.; Nordlander, P.; Halas, N. J. Response to Comment on "Quantifying Hot Carrier and Thermal Contributions in Plasmonic Photocatalysis". *Science* **2019**, *364*, No. eaaw9545.
(36) Seemala, B.; Therrien, A. J.; Lou, M.; Li, K.; Finzel, J. P.; Qi, J.; Nordlander, P.; Christopher, P. Plasmon-Mediated Catalytic O2 Dissociation on Ag Nanostructures: Hot Electrons or Near Fields? *ACS Energy Letters* **2019**, *4*, 1803−1809.
(37) Ma, J.; Gao, S. Plasmon-Induced Electron−Hole Separation at the Ag/TiO_2 (110) Interface. *ACS Nano* **2019**, *13*, 13658−13667.
(38) Sundararaman, R.; Narang, P.; Jermyn, A. S.; Goddard, W. A., III; Atwater, H. A. Theoretical Predictions for Hot-Carrier Generation from Surface Plasmon Decay. *Nat. Commun.* **2014**, *5*, 5788.
(39) Yabana, K.; Bertsch, G. F. Time-Dependent Local-Density Approximation in Real Time. *Phys. Rev. B* **1996**, *54*, 4484−4487.
(40) Gajdo, M.; Eichler, A.; Hafner, J. CO Adsorption on Close-Packed Transition and Noble Metal Surfaces: Trends from Ab Initio Calculations. *J. Phys.: Condens. Matter* **2004**, *16*, 1141−1164.
(41) Moler, E. J.; Kellar, S. A.; Huff, W. R. A.; Hussain, Z.; Chen, Y.; Shirley, D. A. Spatial Structure Determination of $(\sqrt{3}\times\sqrt{3})$R30° and (1.5×1.5)R18° CO orCu(111) Using Angle-Resolved Photoemission Extended Fine Structure. *Phys. Rev. B* **1996**, *54*, 10862−10868.
(42) Hirschmugl, C. J.; Williams, G. P.; Hoffmann, F. M.; Chabal, Y. J. Adsorbate-Substrate Resonant Interactions Observed for Co on Cu(100) and (111) in the Far-Ir Using Synchrotron Radiation. *J. Electron Spectrosc. Relat. Phenom.* **1990**, *54* (55), 109−114.
(43) Raval, R.; Parker, S. F.; Pemble, M. E.; Hollins, P.; Pritchard, J.; Chesters, M. A. FT-rairs, Eels and Leed Studies of the Adsorption of Carbon Monoxide on Cu(111). *Surf. Sci.* **1988**, *203*, 353−377.
(44) Cazalilla, M. A.; Dolado, J. S.; Rubio, A.; Echenique, P. M. Plasmonic Excitations in Noble Metals: The Case of Ag. *Phys. Rev. B* **2000**, *61*, 8033−8042.
(45) Kuisma, M.; Ojanen, J.; Enkovaara, J.; Rantala, T. T. Kohn-Sham Potential with Discontinuity for Band Gap Materials. *Phys. Rev. B* **2010**, *82*, 115106.
(46) Kresse, G.; Hafner, J. Ab Initio Molecular Dynamics for Liquid Metals. *Phys. Rev. B* **1993**, *47*, 558−561.
(47) Kresse, G.; Furthmuller, J. Efficient Iterative Schemes for Ab Initio Total-Energy Calculations Using a Plane-Wave Basis Set. *Phys. Rev. B* **1996**, *54*, 11169−11186.
(48) Kresse, G.; Furthmuller, J. Efficiency of Ab-Initio Total Energy Calculations for Metals and Semiconductors Using a Plane-Wave Basis Set. *Comput. Mater. Sci.* **1996**, *6*, 15−50.
(49) Kresse, G.; Joubert, D. From Ultrasoft Pseudopotentials to the Projector Augmented-Wave Method. *Phys. Rev. B* **1999**, *59*, 1758−1775.
(50) Blochl, P. E. Projector Augmented-Wave Method. *Phys. Rev. B* **1994**, *50*, 17953−17979.
(51) Berland, K.; Hyldgaard, P. Exchange Functional That Tests the Robustness of the Plasmon Description of the van Der Waals Density Functional. *Phys. Rev. B* **2014**, *89*, 035412.
(52) Klimeš, J.; Bowler, D. R.; Michaelides, A. Chemical Accuracy for the van Der Waals Density Functional. *J. Phys.: Condens. Matter* **2009**, *22*, 022201.
(53) Klimeš, J.; Bowler, D. R.; Michaelides, A. Van Der Waals Density Functionals Applied to Solids. *Phys. Rev. B* **2011**, *83*, 195131.
(54) Roman-Perez, G.; Soler, J. M. Efficient Implementation of a van Der Waals Density Functional: Application to Double-Wall Carbon Nanotubes. *Phys. Rev. Lett.* **2009**, *103*, 096102.
(55) Mortensen, J. J.; Hansen, L. B.; Jacobsen, K. W. Real-Space Grid Implementation of the Projector Augmented Wave Method. *Phys. Rev. B* **2005**, *71*, 035109.
(56) Enkovaara, J.; et al. Electronic Structure Calculations with GPAW: A Real-Space Implementation of the Projector Augmented-Wave Method. *J. Phys.: Condens. Matter* **2010**, *22*, 253202.
(57) Larsen, A. H.; Vanin, M.; Mortensen, J. J.; Thygesen, K. S.; Jacobsen, K. W. Localized Atomic Basis Set in the Projector Augmented Wave Method. *Phys. Rev. B* **2009**, *80*, 195112.
(58) Kuisma, M.; Sakko, A.; Rossi, T. P.; Larsen, A. H.; Enkovaara, J.; Lehtovaara, L.; Rantala, T. T. Localized Surface Plasmon Resonance in Silver Nanoparticles: Atomistic First-Principles Time-Dependent Density-Functional Theory Calculations. *Phys. Rev. B* **2015**, *91*, 115431.
(59) Gritsenko, O.; van Leeuwen, R.; van Lenthe, E.; Baerends, E. J. Self-Consistent Approximation to the Kohn-Sham Exchange Potential. *Phys. Rev. A* **1995**, *51*, 1944.
(60) Lehtola, S.; Steigemann, C.; Oliveira, M. J. T.; Marques, M. A. L. Recent Developments in Libxc — A Comprehensive Library of Functionals for Density Functional Theory. *SoftwareX* **2018**, *7*, 1−5.
(61) Larsen, A. H.; et al. The Atomic Simulation Environment—a Python Library for Working with Atoms. *J. Phys.: Condens. Matter* **2017**, *29*, 273002.
(62) Harris, C. R.; et al. Array Programming with NumPy. *Nature* **2020**, *585*, 357−362.
(63) Virtanen, P.; et al. SciPy 1.0: Fundamental Algorithms for Scientific Computing in Python. *Nat. Methods* **2020**, *17*, 261−272.
(64) Hunter, J. D. Matplotlib: A 2D Graphics Environment. *Computing in Science Engineering* **2007**, *9*, 90−95.
(65) Humphrey, W.; Dalke, A.; Schulten, K. VMD: Visual Molecular Dynamics. *J. Mol. Graphics* **1996**, *14*, 33−38.
(66) Stone, J. An Efficient Library for Parallel Ray Tracing and Animation. M.Sc. Thesis, Computer Science Department, University of Missouri-Rolla, 1998.
(67) Molder, F.; Jablonski, K. P.; Letcher, B.; Hall, M. B.; Tomkins-Tinch, C. H.; Sochat, V.; Forster, J.; Lee, S.; Twardziok, S. O.; Kanitz, A.; Wilm, A.; Holtgrewe, M.; Rahmann, S.; Nahnsen, S.; Koster, J. Sustainable Data Analysis with Snakemake. *F1000Research* **2021**, *10*, 33.

https://doi.org/10.1021/acs.nanolett.2c02327
Nano Lett. XXXX, XXX, XXX−XXX

Supporting Information

Hot-carrier transfer across a nanoparticle-molecule junction: The importance of orbital hybridization and level alignment

Jakub Fojt[1], Tuomas P. Rossi[2], Mikael Kuisma[3], and Paul Erhart[1]

[1] *Department of Physics, Chalmers University of Technology, SE-412 96 Gothenburg, Sweden*
[2] *Department of Applied Physics, Aalto University, FI-00076 Aalto, Finland*
[3] *Department of Physics, Technical University of Denmark, DK-2800 Kongens Lyngby, Denmark*

Contents

Supplementary Figures

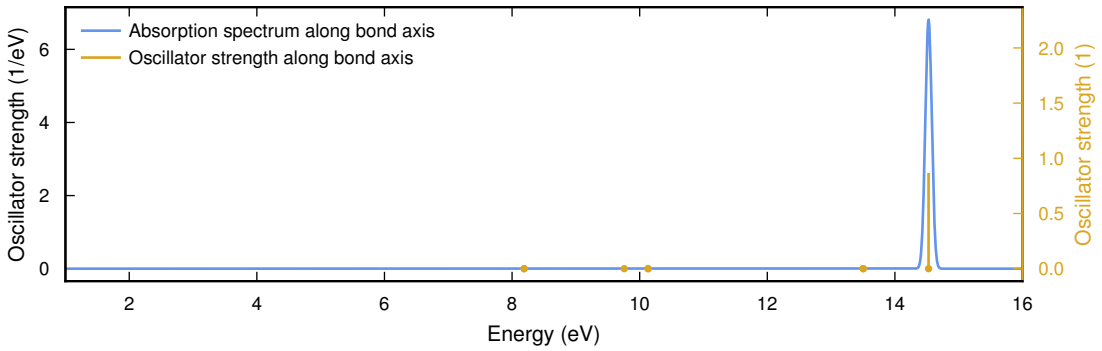

Figure S1: **Absorption spectrum of free CO molecule along its bond axis.** The free CO molecule (bond length 1.144 Å) has its first excited state at 8.19 eV. This is an optically dark state that corresponds to the HOMO-LUMO transition. The first bright state is 14.53 eV. The transitions were obtained by linear response TDDFT calculations in GPAW with the xc-functional PBE.

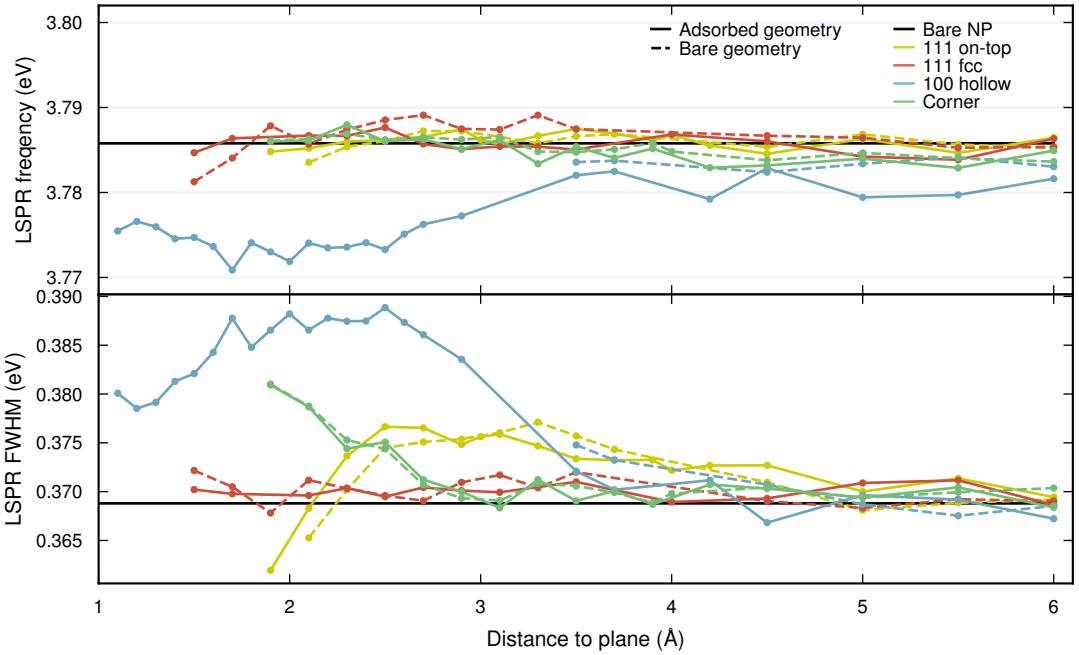

Figure S2: **Frequency and width of Ag_{201} LSP.** The bare NP has a LSP frequency close to 3.8 eV (determined by fitting a Lorentizan function to the spectrum). Adding the CO molecule shifts the LSP frequency by less than 15 meV for the 100 hollow site, and less than 5 meV for the other sites.

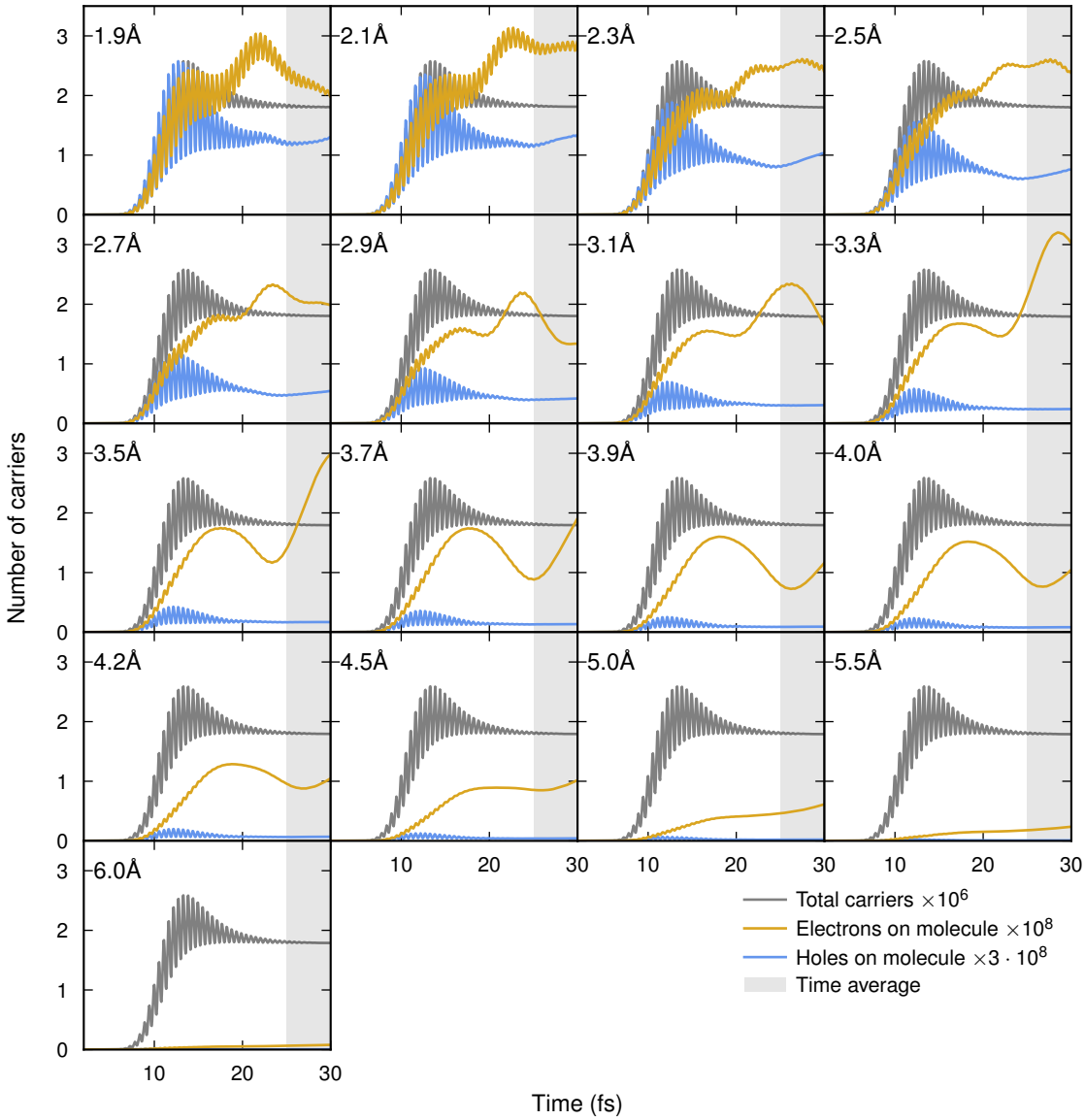

Figure S3: **HC generation in Ag_{201} with the CO in (111) on-top configuration..** The total amount of carriers in the NP + CO, the number of electrons in the CO and the number of holes in the CO are shown as a function of time after excitation with pulse of frequency 3.8 eV. While the total number of carriers in the system stabilizes before the end of the simulation, the number of electrons (in particular) and holes exhibits some oscillations. The oscillations stem from the dynamics between several electron-hole excitations between hybridized NP-molecule states. We note that an apparent maximum occurs in the number of transferred electrons close to the end of the simulation, and that this maximum occurs faster with closer distances (stronger coupling between NP and molecular states). The time span in which time averages are taken elsewhere in the paper (25 to 30 fs) is highlighted in the figure. For all but the intermediate distances, taking the average yields similar results to taking the values at the end of the simulation.

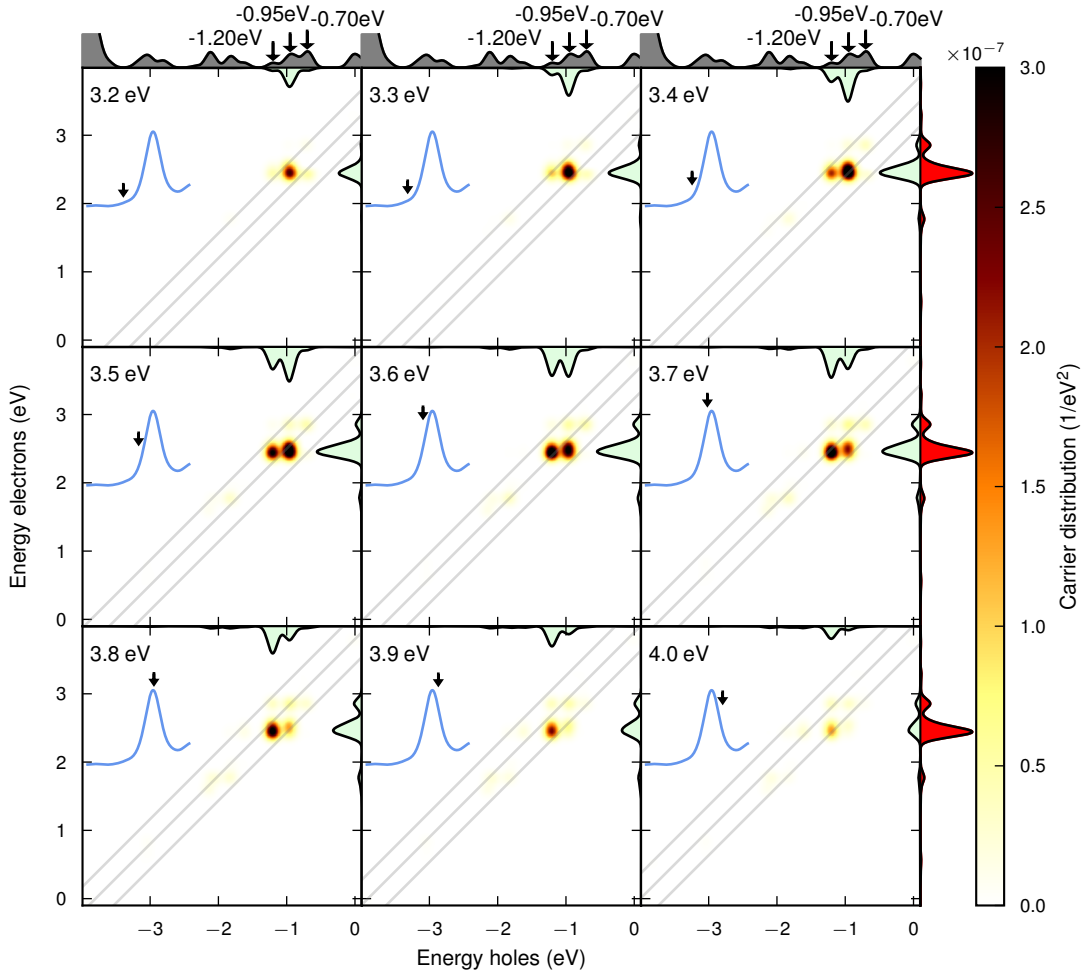

Figure S4: **Decomposition of electrons generated on the molecule in electrons and holes, depending on pulse frequency.** The quantity $\sum_{ia} M_{ia} w^{(\mathrm{mol})}_{aa'} \delta(\varepsilon - \varepsilon_a)\delta(\varepsilon - \varepsilon_i)$ where $M_{ia} = \sum_{a'}^{f_i > f_a, f_i > f_{a'}} (q_{ia} q_{ia'} + p_{ia} p_{ia'})$ shows a map between holes (in the combined system NP+CO) and electrons in the CO molecule, for a particular geometry (Ag_{201} (111) on-top distance 3.3 Å) at 30 fs in the simulation. The map with hole/electron dependence integrated out ($\sum_{ia} M_{ia} w^{(\mathrm{mol})}_{aa'} \delta(\varepsilon - \varepsilon_a) / \sum_{ia} M_{ia} w^{(\mathrm{mol})}_{aa'} \delta(\varepsilon - \varepsilon_i)$) is shown on the inner axes in a fixed scale. DOS of the combined system and PDOS of the molecule are shown on the outer axes. The inset of the optical spectrum shows the pulse frequency used. The electron transfer involves primarily occupied states at three energies (−1.2, −0.95 and −0.7 eV) and unoccupied states in the molecule at three levels. As involved states need to be resonant ($\varepsilon_a - \varepsilon_i = \hbar\omega_{\mathrm{pulse}}$, indicated by the middle diagonal line, while the outer diagonal lines indicate the half-width at half-maximum of the pulse 0.37 eV) the contribution of each state varies with pulse frequency. Maximum electron transfer is achieved at 3.5-3.6 eV, slightly off the LSP resonance, when the states at −1.2 and −0.95 eV are resonant with the main LUMO branch. The former states occupied states are thus interacting more strongly with the transfer to the LUMO than the states at −0.7 eV.

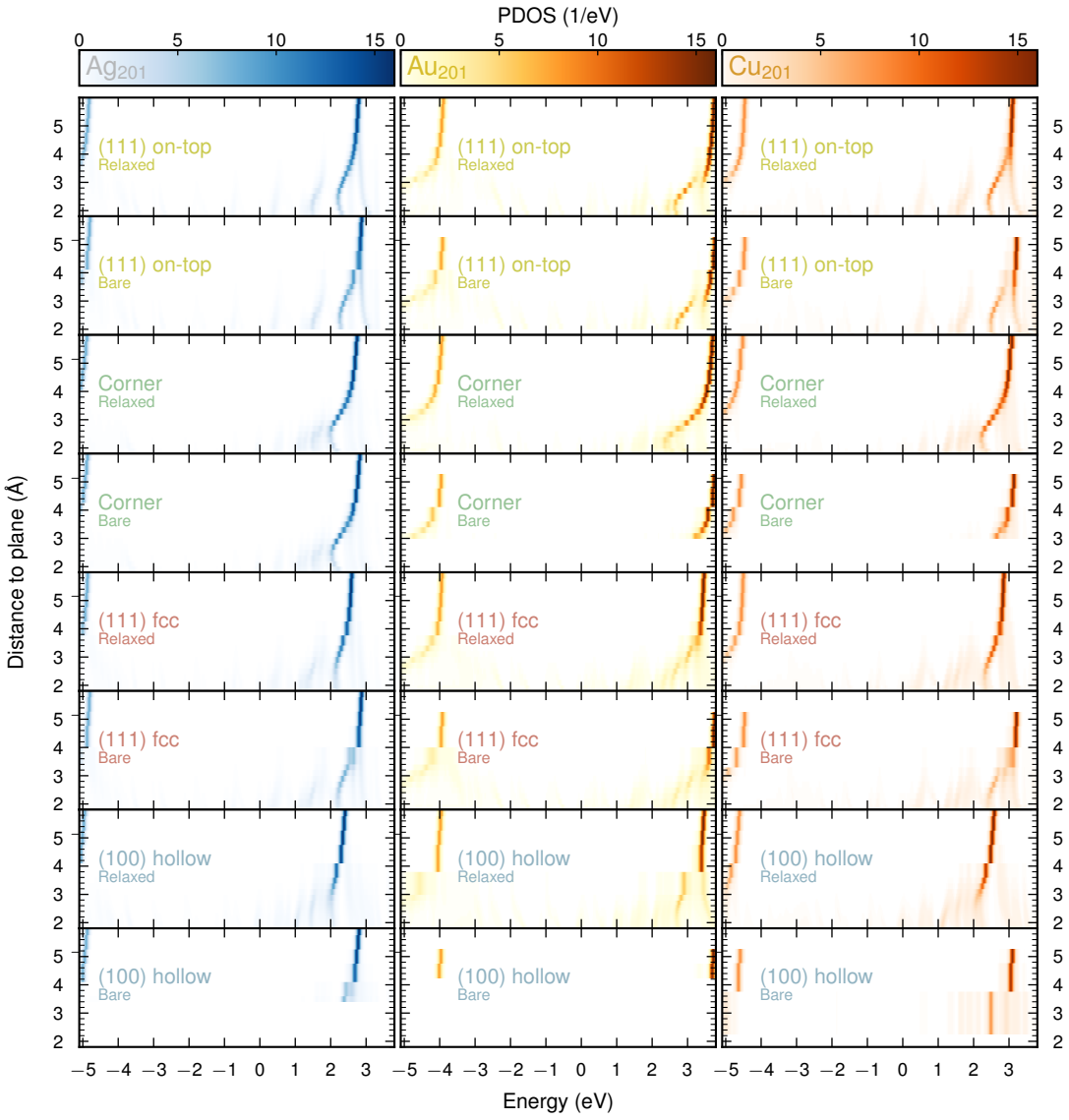

Figure S5: **Projected density of states for the molecule, in the combined system.** As the molecule is brought closer to the NP, the HOMO and LUMO orbitals shift to lower energies (distance 4 to 6 Å) and hybridize, splitting up into several branches (distances smaller than 4 Å).

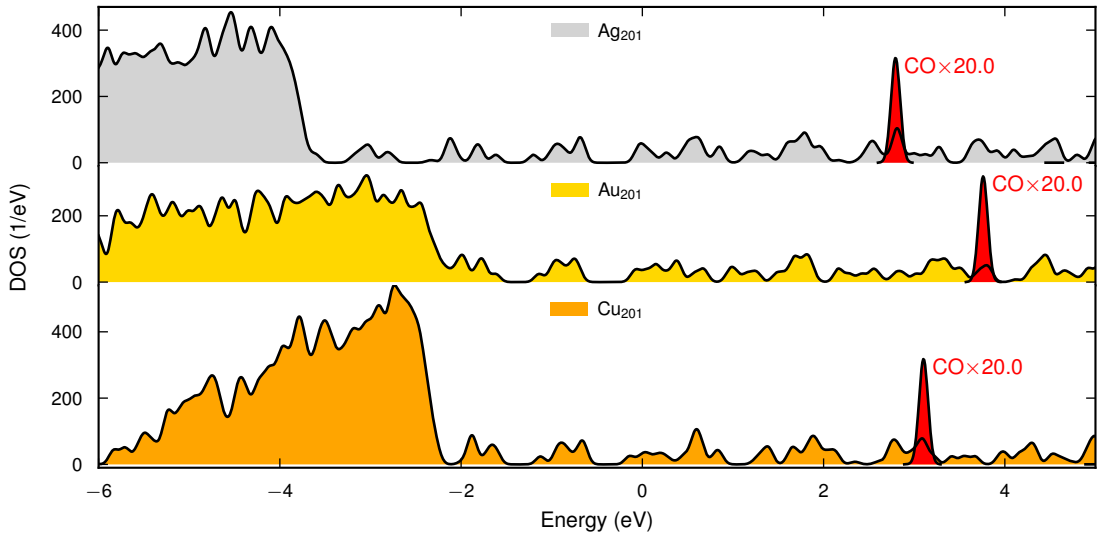

Figure S6: **Density of states of Ag_{201}, Au_{201}, and Cu_{201}.** The DOS is shown relative to Fermi level, and the PDOS of the molecule at far distances is included in the figure, showing its alignment to the different metals.

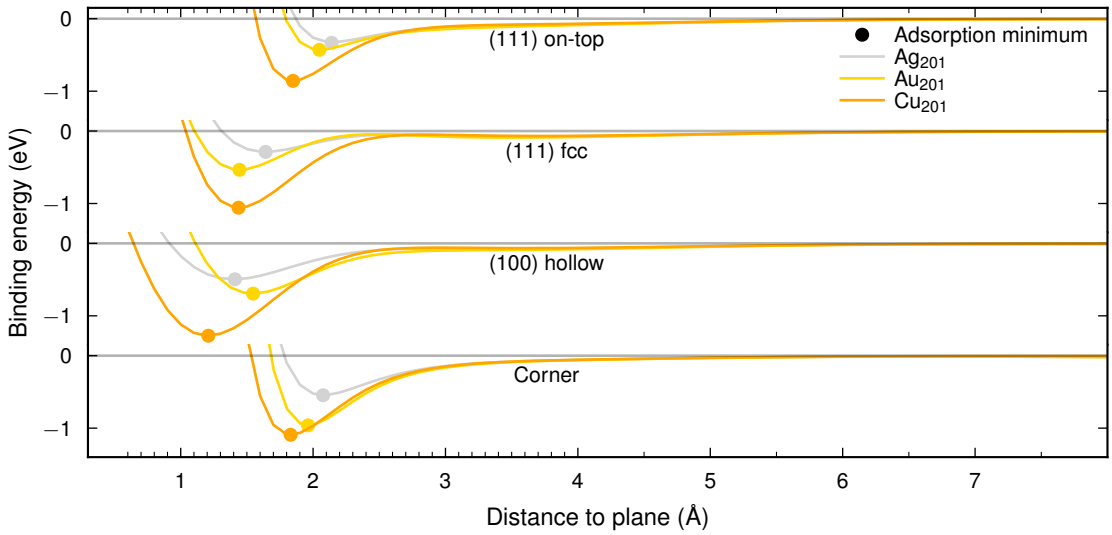

Figure S7: **Binding energies of the combined CO + NP system as a function of site and distance.** Energies are computed in VASP using the vdW-cx-df xc-functional. The molecule is rigidly displaced from its adsorption minimum without allowing neither the bond length nor the NP to relax. The binding energy is defined $E^{(\mathrm{site})}_{\mathrm{bind}}(d) = E^{(\mathrm{site})}(d) - E^{(\mathrm{site})}_{\mathrm{NP}} - E^{(\mathrm{site})}_{\mathrm{mol}}$ where $E^{(\mathrm{site})}_{\mathrm{NP}}$ ($E^{(\mathrm{site})}_{\mathrm{mol}}$) is the energy of the system, in its adsorbed configuration, without the molecule (NP). Ticks in the distance axis mark points distances sampled.

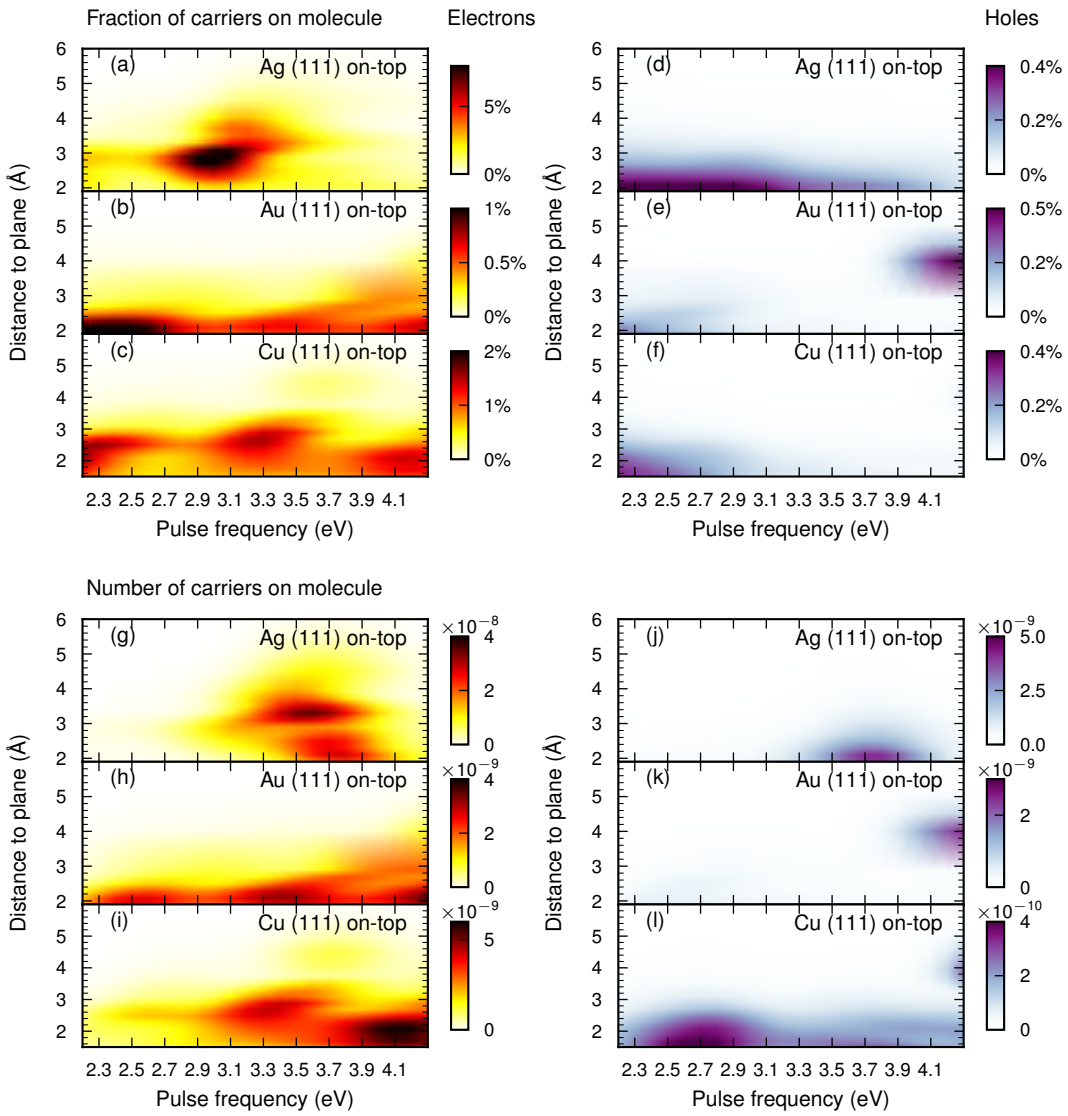

Figure S8: **Pulse-frequency dependence of the electron generation in CO.** The amount of electrons (a-c, g-i) and holes (d-f, j-l) generated on the molecule is expressed as a fraction of carriers (a-f; number of carriers on molecule divided by number of carriers in the combined system) and as a number (g-l). The numbers of generated carriers are computed as the average between 25 and 30 fs in the simulation.

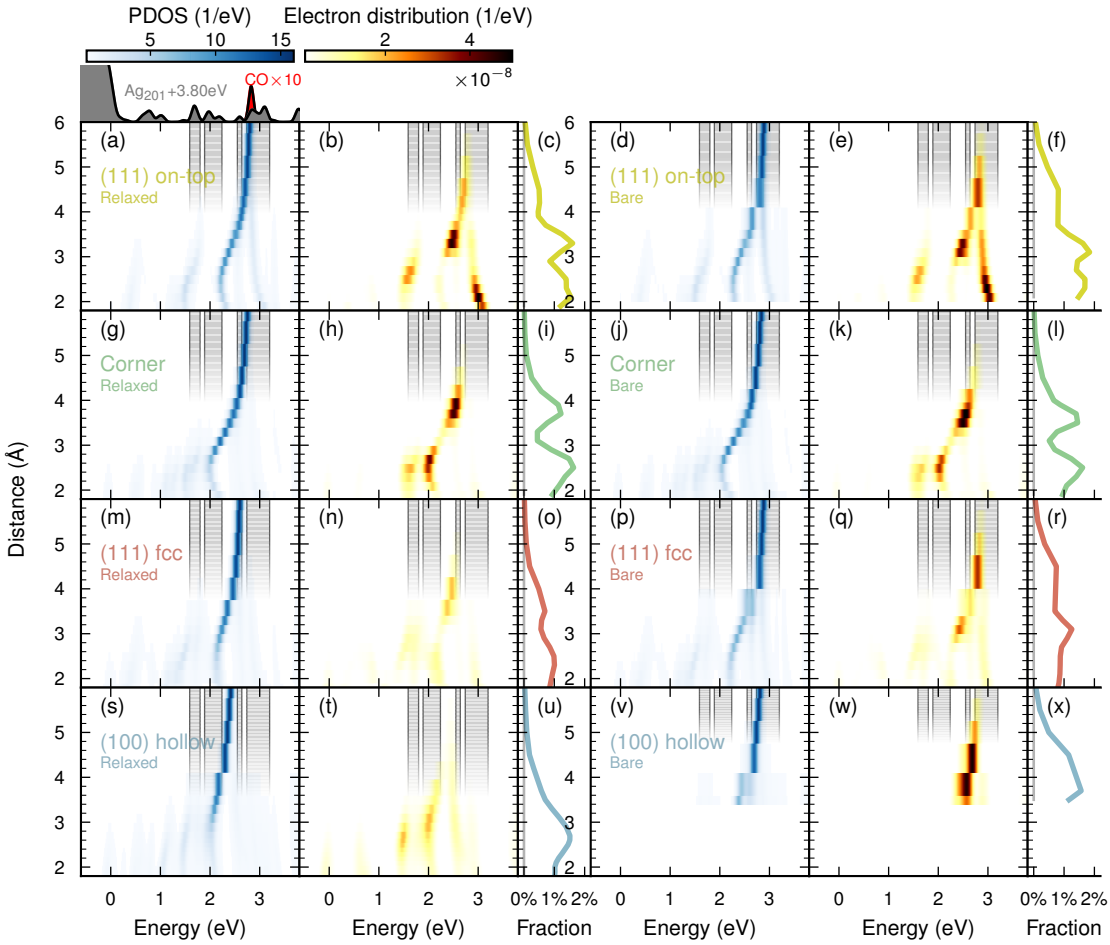

Figure S9: **Level alignment between the projected densities of state of the NP and molecule for Ag_{201}.** "Relaxed" refers to the combined system that has been relaxed in the adsorption minimum, and the molecule then shifted. "Bare" refers to the NP being configured as the free NP and the CO with the bond length of the free CO molecule. For the two types of geometries, the molecular PDOS differs primarily by a constant shift of the LUMO orbital energy (most apparent for the (111) fcc and (100) hollow sites). The shift in PDOS changes the resonance condition, and thus the electron distribution on the molecule and fraction of electrons generated on the molecule. The electron distributions are computed as the average between 25 and 30 fs in the simulation for the Ag_{201} (111) on-top configuration.

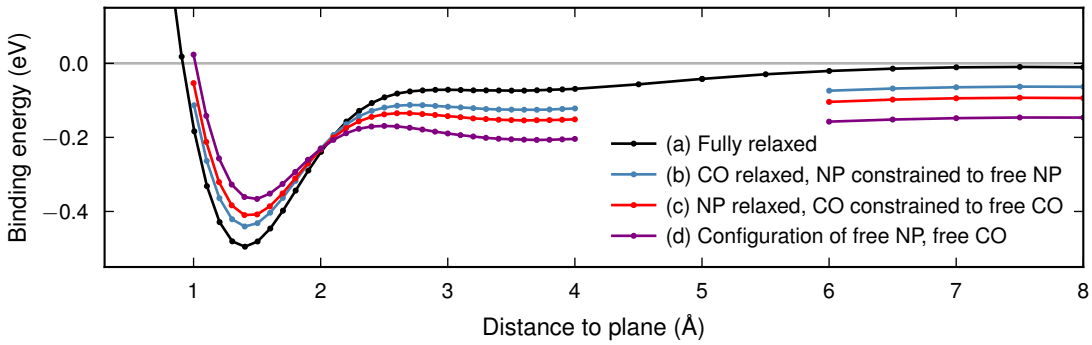

Figure S10: **Binding energies of CO + Ag_{201} under constrained relaxation.** The binding energy is defined $E_{\mathrm{bind}}^{(\mathrm{site})}(d) = E^{(\mathrm{site})}(d) - E_{\mathrm{NP}}^{(\mathrm{site})} - E_{\mathrm{mol}}^{(\mathrm{site})}$ where $E_{\mathrm{NP}}^{(\mathrm{site})}$ ($E_{\mathrm{mol}}^{(\mathrm{site})}$) is the energy of the system, in its adsorbed configuration, without the molecule (NP). Binding energies are computed by rigidly displacing the CO along a line from the (111) on-top site of the NP, from 4 different starting positions. The starting positions are:
(a) The combined system (NP and CO) is fully relaxed in the adsorption minimum (same as in Fig. S7.
(b) The combined system is relaxed with a constraint: all Ag atoms are fixed in the positions of the free NP.
(c) The combined system is relaxed with a constraint: the CO bond length is fixed to the bond length of the free molecule.
(d) The combined system is not relaxed. The configuration of a free NP and free molecule are used.
Of the 4 options fully relaxing the system (a) gives the lowest energies close to the adsorption minimum, but the highest in the long-distance limit, which is expected. Taking the free NP and free molecule configurations (d) gives the highest energies close to the adsorption minimum and the lowest in the long-distance limit. The relaxation of the molecule only (b; the bond length increases compared to the bond length of free CO) and of the NP only (c; which manifests itself as distortion of the NP surface close to the CO) contribute roughly equally to the energies. In principle finding a minimum energy path over the entire range of distances can be done, by performing a constrained relaxation at every distance. Such a calculation would yield a curve that is at every distance lower in energy than any other curve, effectively widening the adsorption minimum. Note that as the reference $E_{\mathrm{NP}}^{(\mathrm{site})}$, and $E_{\mathrm{mol}}^{(\mathrm{site})}$ are taken for the fully relaxed configurations binding energies at long distances are negative for options (b-d); this is the expected behavior for our definition of binding energy.

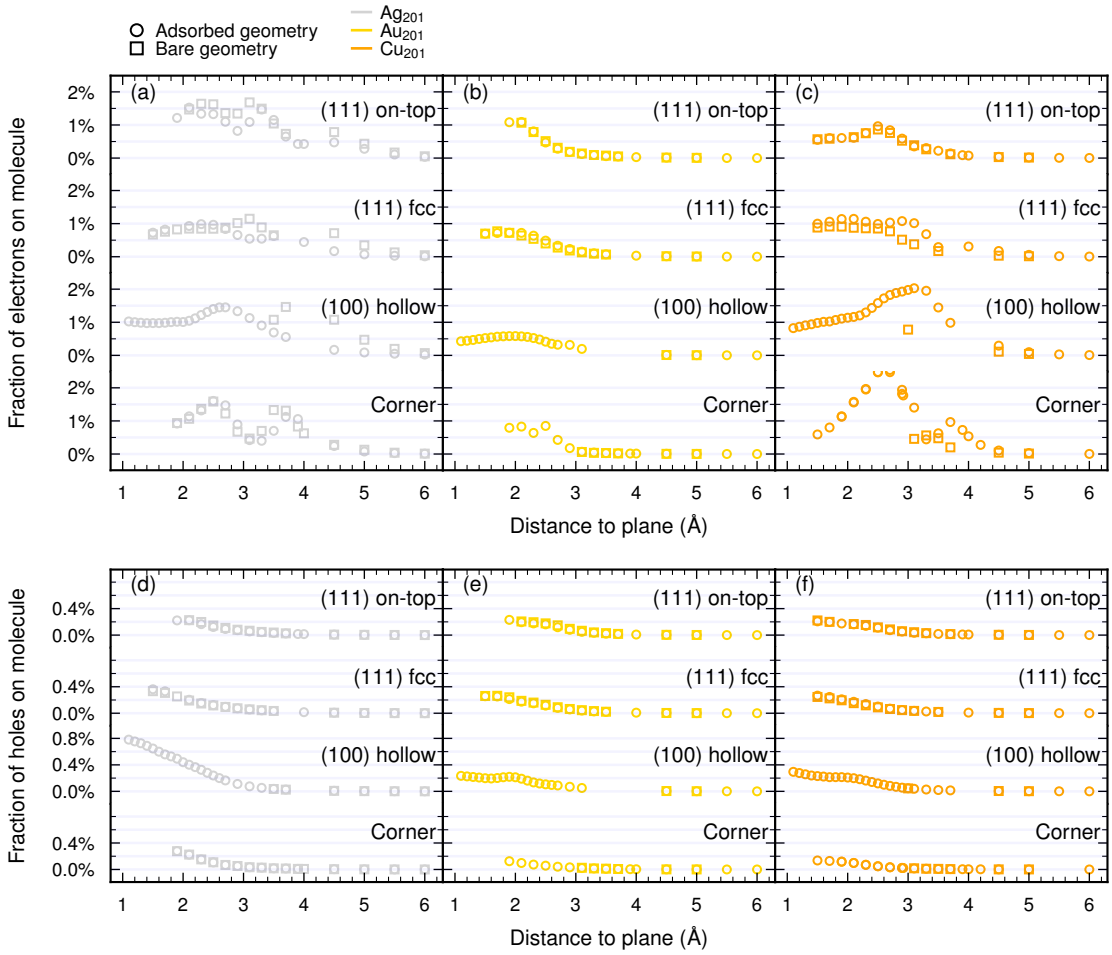

Figure S11: **Carrier generation on the molecule after plasmon decay.** Electrons (a-c) and holes (d-f) generated in Ag_{201} (a, d), Au_{201} (b, e), Cu_{201} (c, f) for the considered sites, distances, and geometrical configurations. "Adsorbed geometry" refers to the combined system that has been relaxed in the adsorption minimum, and the molecule then shifted. "Bare geometry" refers to the NP being configured as the free NP and the CO with the bond length of the free CO molecule. For the two types of geometries, the curves are similar for the electrons (with the exception of a few features), and practically identical for the holes. The differences for the electrons are explained by the shift in the CO LUMO orbital due to changing bond length, which affects the resonance condition (Fig. S9). Pulse frequencies are 3.8 eV (Ag), 2.5 eV (Au) and 2.7 eV (Cu). The fractions of generated carriers are computed as the average between 25 and 30 fs in the simulation.

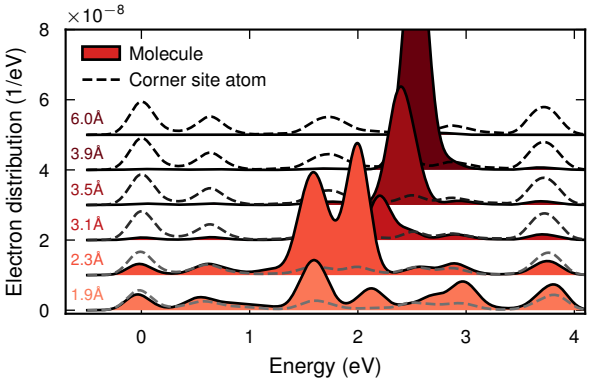

Figure S12: **Energy distribution of electrons generated on the molecule and on the NP corner site that the molecule approaches.** While the former varies non-monotonically, the latter is practically unchanged with distance.

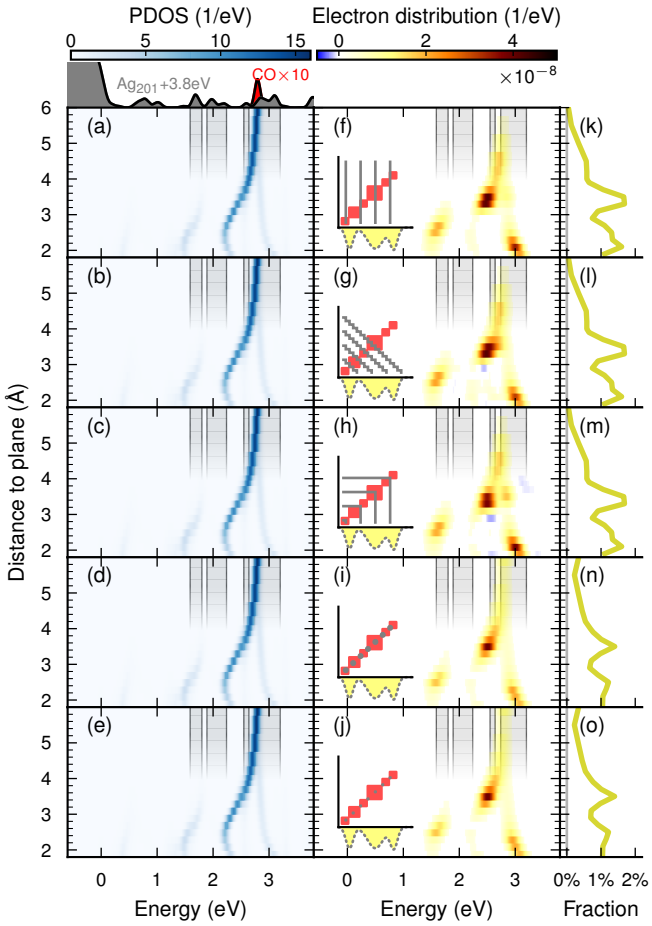

Figure S13: **Alternative formulations of electron distribution in molecule after plasmon decay.** The electron distribution in the molecule is well defined as a sum over unoccupied-unoccupied space $P_{\mathrm{e}}^{(\mathrm{mol})}(\boldsymbol{r}) = \frac{1}{2}\sum_{aa'} M_{aa'} w_{aa'}^{(\mathrm{mol})}$ of the density matrix product $M_{aa'} = \sum_i^{f_i>f_a, f_i>f_{a'}} (q_{ia}q_{ia'} + p_{ia}p_{ia'})$, $w_{aa'}^{(\mathrm{mol})} = \int_{\mathrm{mol}} \psi_a^{(0)}(\boldsymbol{r})\psi_{a'}^{(0)}(\boldsymbol{r})\mathrm{d}\boldsymbol{r}$. Simultaneous resolution in energy is not unambiguously defined. (a-e) PDOS on the molecule as a function of distance. All panels are identical. (f-j) Electron distribution expressed as (f) row/column-wise summation $\sum_{aa'} M_{aa'} w_{aa'}^{(\mathrm{mol})} \delta(\varepsilon - \varepsilon_a)$. (g) energy average summation $\sum_{aa'} M_{aa'} w_{aa'}^{(\mathrm{mol})} \delta(\varepsilon - \frac{\varepsilon_a + \varepsilon_{a'}}{2})$. (h) wedge-shape summation $\sum_{aa'} M_{aa'} w_{aa'}^{(\mathrm{mol})} \delta(\varepsilon - \max(\varepsilon_a, \varepsilon_{a'}))$. (i) degenerate-eigenvalue summation $\sum_{aa'} M_{aa'} w_{aa'}^{(\mathrm{mol})} \delta(\varepsilon - \varepsilon_a)\delta(\varepsilon_a - \varepsilon_{a'})$. (j) diagonal-only summation $\sum_{aa'} M_{aa'} w_{aa'}^{(\mathrm{mol})} \delta(\varepsilon - \varepsilon_a)\delta_{aa'}$. Note that between the forms (f-h) the distribution varies only slightly, however with some negative (unphysical) contributions to (g-h). (k-o) Energy integral of the distributions (f-j). For all but the diagonal-only and degenerate eigenvalues summation the end results are identical. The electron distributions are computed at 30 fs in the simulation for the Ag_{201} (111) on-top configuration.

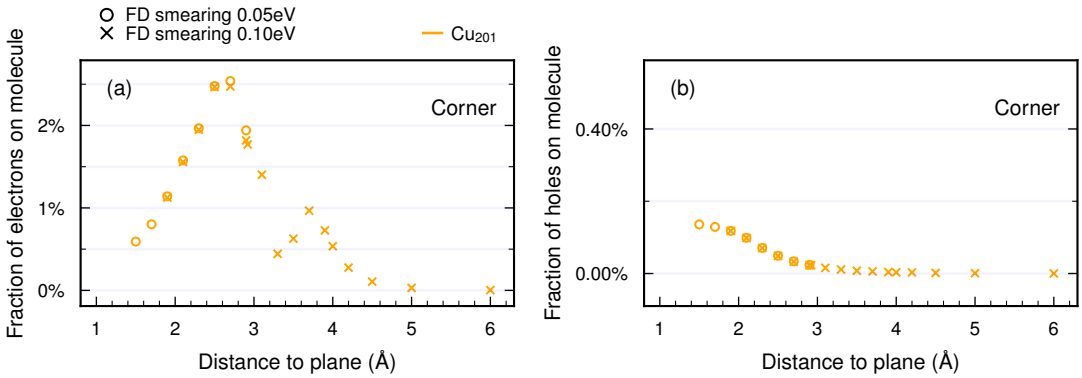

Figure S14: **Carrier generation depending on occupation number smearing.** We compare the fraction of electrons (a) and holes (b) generated on the molecule for the corner site of the Cu_{201} NP. Fermi-Dirac occupation number smearing with the parameters 0.05 eV and 0.1 eV was used. Data is not available at certain distances for the lower value of the smearing parameter (as SCF cycle convergence was difficult to reach with the GLLB-SC xc-functional) but is otherwise in good agreement with the higher parameter value. The fractions of electrons are computed as the average between 25 and 30 fs in the simulation for the Ag_{201} (111) on-top configuration.

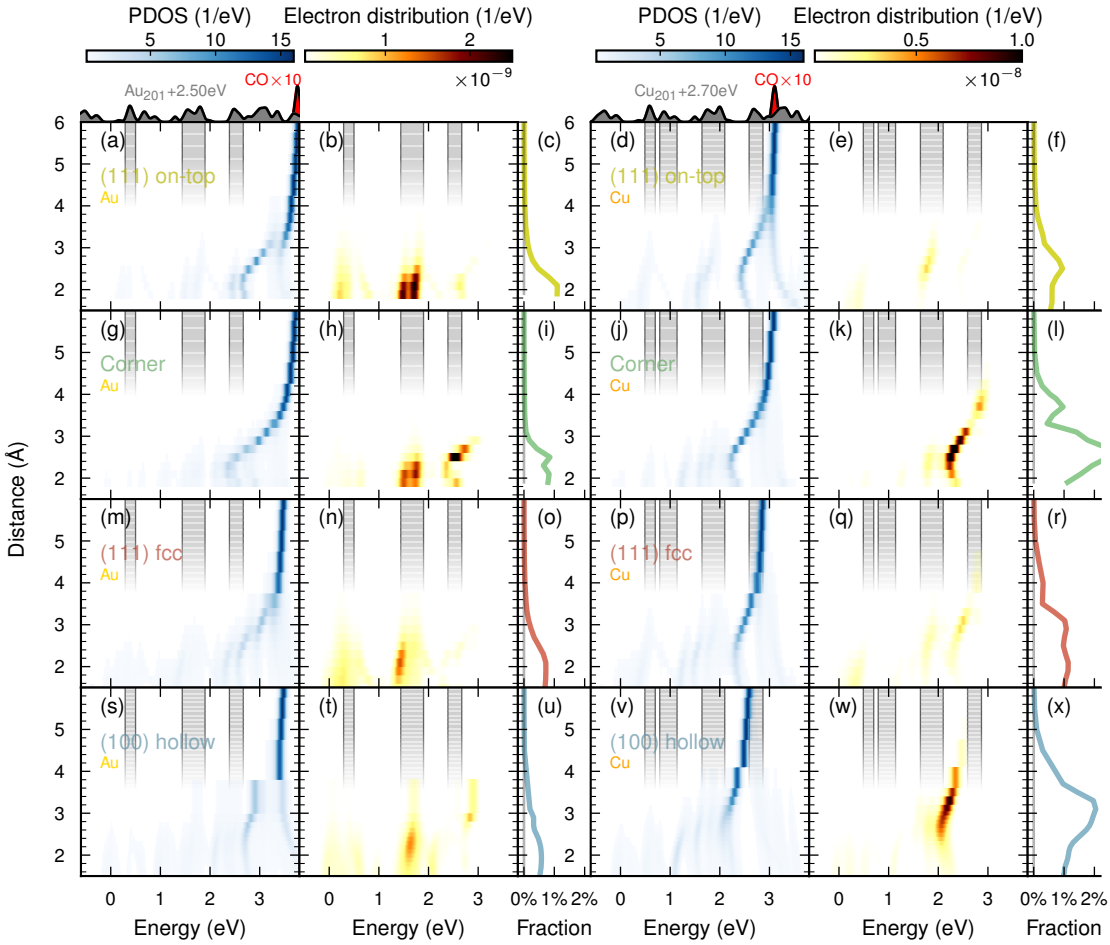

Figure S15: **Level alignment between the projected densities of state of the NP and molecule for Au_{201} and Cu_{201}.** The electron distributions are computed as the average between 25 and 30 fs in the simulation for the Ag_{201} (111) on-top configuration.

Supplementary Tables

Table S1: **Summary of binding energies, vibrational frequencies and associated bond distances.** Vibrational frequencies of the metal-C bond were computed by fitting a Morse potential to the binding energy curves (Fig. S7). Binding energies are here given as positive quantities $E_{\mathrm{NP}} + E_{\mathrm{mol}} - E_{\mathrm{NP+mol}}$. Data computed in this work, in other theoretical work (Ref. 1) and from experiment (Refs. 2, 3 and 4) is presented. The agreement is good where data is available.
TW: This work. Lit.: Literature.

	C-O distance (Å)		Metal-C distance (Å)		Metal-C frequency (cm^{-1})		Binding energy (meV)	
Ag_{201}	TW	Lit.	TW	Lit.	TW	Lit.	TW	Lit.
(111) on-top	1.151	1.150[1]	2.1	2.2[1]	203	203[1]	295	160[1]
(111) fcc	1.170	1.168[1]	1.6	1.6[1]	176		215	80[1]
(100) hollow	1.184		1.4		163		356	
corner	1.150		2.1		250		531	
Au_{201}								
(111) on-top	1.148	1.150[1]	2.0	2.1[1]	244		351	320[1]
(111) fcc	1.180	1.178[1]	1.4	1.4[1]	245		316	300[1]
(100) hollow	1.176		1.5		225		522	
corner	1.152		2.0		347		894	
Cu_{201}								
(111) on-top	1.158	1.156[1]	1.8	2.0[1]/1.9[2]	338	323[1]/346[3]/331[4]	787	750[1]
(111) fcc	1.183	1.179[1]	1.4	1.4[1]	286		929	880[1]
(100) hollow	1.205		1.2		232		1058	
corner	1.155		1.8		355		1002	

Supplementary Notes

Supplementary Note S1: Geometry of atomic structures

In this work we study the regular truncated octahedron (RTO)-shaped Ag_{201}, Au_{201}, and Cu_{201} nanoparticles (NPs). The RTO shape is consistent with an ideal face-centered cubic (fcc) lattice that has been truncated so that it has eight {111} surfaces and six {100} surfaces. We identify four molecular adsorption sites on the NP. On the (111) surface we consider the center on-top site and its nearest fcc site. We also consider the hollow site closest to the center of the (100) face, and the corner site between a {100} and two {111} surfaces. In each site the immediate environment of the molecule is different; it has one nearest-neighbor metal atom for the (111) on-top and corner sites, three for the (111) fcc site and four for the (100) hollow site.

We place a CO molecule (C facing the metal) near each site and find minimum energy configurations by allowing all metal and molecule atoms to relax. In the relaxed configurations (Table S1) the bond length and NP-molecule distance are thus different for each site. The bond length of CO, which is 1.144 Å in the free molecule, increases when adsorbed to the NP. Higher coordination numbers for the C atom thus result in larger bond lengths. This is in agreement with previous studies on the extended (111) Ag surface[1], and can be understood by considering that as C shares more electron density in bonds with metal atoms, the CO bond is weakened.

We study the distance dependence by rigidly shifting the molecule from the adsorbed configuration, i.e., without changing the CO bond length or the positions of the metal atoms. The shift is performed along a line perpendicular to the respective surface for the (111) and (100) sites and along the line through the opposing corner site for the corner site. We note that at long separations such rigidly shifted configurations are relatively high in energy. Specifically, at long distances the minimum energy configuration would be a molecule with the bond length of bare CO and a fully relaxed bare NP. In general, finding such minimum energy configurations under a distance constraint is a highly multidimensional problem. We therefore limit our discussion to rigid translations of the molecule, without compromising our conclusions (Fig. S9).

As we vary the NP-CO distance, we observe minima in the binding energy curves around 250 meV to 500 meV at 1.5 Å-2.3 Å (Fig. S7). Distances corresponding to energy minima as well as the computed vibrational frequencies (Table S1) are in good agreement with earlier calculations[1] and experiment[2–4]. Here, we define the binding energy as

$$E_{\mathrm{bind}}^{(\mathrm{site})}(d) = E^{(\mathrm{site})}(d) - E_{\mathrm{NP}}^{(\mathrm{site})} - E_{\mathrm{mol}}^{(\mathrm{site})}, \tag{S1}$$

where $E_{\mathrm{NP}}^{(\mathrm{site})}$ and $E_{\mathrm{mol}}^{(\mathrm{site})}$ are the energies of the NP and molecule, respectively, taken from two separate calculations, representing infinite separation. Note that in this definition (Eq. S1), we take $E_{\mathrm{NP}}^{(\mathrm{site})}$ and $E_{\mathrm{mol}}^{(\mathrm{site})}$ as the energies of the NP and molecule as in the relaxed configuration for the specific site, emphasized by the superscript (site). Allowing the molecule to relax at each distance effectively widens the adsorption curve but does not affect the main conclusions drawn in our work (Fig. S10, Fig. S11). Fixing the bond length reduces, however, the degrees of freedom and simplifies the discussion, whence we adopt this constraint here.

In our work we find that the hot carrier (HC) transfer landscape has a detailed structure. It is then important to remember that in reality both the molecule and the NP are subjected to thermal motion. Since it is the weakest interaction in the combined system, one can expect the relative motion of NP and molecule to have the most pronounced thermal effect on level alignment, effectively broadening the peaks in the HC transfer probability curves. Considering $kT \approx 25$ meV at room temperature and the calculated binding energy curves (Fig. S7), we should expect the molecule to move much less than 1 Å along the distance axis, but in reality the molecule is free to move laterally as well as rotate. Sampling the landscape of HC transfer in the full space of molecular movement is a high-dimensional problem that can be addressed in future work.

Supplementary Note S2: Comparison of across-interface electron generation to surface electron distribution

We emphasize that the energy distribution of electrons generated on the molecule depends on energetic level alignment of the molecular levels, by computing the energy distribution of electrons on the nearest metal atom (the integral of Eq. S22 in the metal-atom Voronoi cell) as a function of distance (Fig. S12). We focus specifically on the corner site, where the distance dependence of the electron distribution on the molecule exhibits two clear maxima. We find that the electron distribution on the adsorption site is practically distance-independent.

Only at the smallest considered distances does the electron distribution on the molecule resemble the electron distribution at the adsorption site on the metal. Hence it is not enough to know the electron distribution on surfaces and surface sites for a bare NP to predict across-interface electron generation in combined NP + molecule systems. Equipped with distributions for the bare NP alone one misses for example that about 2 times more electrons are generated at 2.5 Å for the corner site, than at 1.9 Å. In other words, the surface electron distribution is an insufficient predictor for across-interface electron generation.

Supplementary Note S3: Methodology

In the limit of weak perturbation, the system response can be assumed to be linear. This means that the Fourier transform of the *response* at one particular frequency depends only on the Fourier transform of the *perturbation* at the same frequency, and the linear response to a time-dependent perturbation can be retrieved knowing the linear impulse response. Similarly to Ref. 5, we use this property in real-time time-dependent density functional theory (RT-TDDFT) to compute optical spectra and model hot-carrier generation in arbitrary weak electric fields. For simplicity we adopt Hartree atomic units in this section.

Plasmonic response in the δ-kick technique

In the δ-kick technique[6] the time-dependent external potential is set to a kick in the z-direction of strength K_z

$$v_{\text{ext}}(\boldsymbol{r}, t) = K_z z \delta(t), \tag{S2}$$

and the system is allowed to evolve in time.

We define the induced density due to the δ-kick $\delta n^{\text{kick}}(\boldsymbol{r}, t) = n^{\text{kick}}(\boldsymbol{r}, t) - n(\boldsymbol{r}, 0)$ and the induced dipole moment in the z-direction as

$$\delta\mu_z^{\text{kick}}(t) = \mu_z^{\text{kick}}(t) - \mu_z(0) = \int \mathrm{d}\boldsymbol{r}\delta n^{\text{kick}}(\boldsymbol{r}, t) z. \tag{S3}$$

The optical spectrum in the z direction can then be expressed via the dipole strength function

$$S_z(\omega) = -\frac{2\omega}{\pi}\Im\left[\frac{\mu_z(\omega)}{K_z}\right], \tag{S4}$$

where $\mu_z(\omega)$ is the Fourier transform of $\mu_z(t)$.

Carrier generation in the δ-kick technique

In Kohn-Sham (KS)-RT-TDDFT the KS density operator

$$\rho(t) = \sum_k |\phi_k(t)\rangle\, f_k\, \langle\phi_k(t)| \tag{S5}$$

contains all information about the system. Here, $\phi_k(t)$ are the KS wave functions at time t and f_k their ground state occupation numbers. In practice, the operator is expressed as the KS density matrix

in the basis of ground state wave functions $|\phi_k^{(0)}\rangle = |\phi_k(0)\rangle$

$$\rho_{nn'}(t) = \langle\phi_n^{(0)}|\,\rho(t)\,|\phi_{n'}^{(0)}\rangle \tag{S6}$$

$$= \sum_k \langle\phi_n^{(0)}|\,|\phi_k(t)\rangle\, f_k\, \langle\phi_k(t)|\,|\phi_{n'}^{(0)}\rangle\,. \tag{S7}$$

In linear response we can express the KS density matrix $\rho_{nn'}(t)$ corresponding to an arbitrary time-dependent field $\boldsymbol{\mathcal{E}}(t)$ in terms of the KS density matrix $\rho_{nn'}^{\mathrm{kick}}(t)$ due to the δ-kick

$$\rho_{nn'}(\omega) = \frac{1}{K_z}\rho_{nn'}^{\mathrm{kick}}(\omega)\mathcal{E}_z(\omega). \tag{S8}$$

Here, functions of ω are Fourier transforms of the corresponding time-dependent quantities, and we have constrained ourselves to fields where the z-component $\mathcal{E}_z$ is the only non-zero component of $\boldsymbol{\mathcal{E}}$. By the convolution theorem Eq. S8 is equivalent to

$$\rho_{nn'}(t) = \frac{1}{K_z}\int_0^\infty \mathrm{d}\tau\rho_{nn'}^{\mathrm{kick}}(\tau)\mathcal{E}_z(t-\tau). \tag{S9}$$

In practice, we compute the Fourier transform of the KS density matrix during the time propagation with the δ-kick and obtain the response to other fields as a post-processing step, using Eq. S8 and inverse Fourier transformation.

To compute the distributions of generated carriers we follow the method of Ref. 5, where expressions that include second-order corrections to the density matrix are derived. For notational convenience (see Supplementary Note 2 of Ref. 5), we introduce the notation

$$q_{ia}(t) = 2\Re\delta\rho_{ia}(t)/\sqrt{2(f_i - f_a)} \tag{S10}$$

$$p_{ia}(t) = -2\Im\delta\rho_{ia}(t)/\sqrt{2(f_i - f_a)}, \tag{S11}$$

which is well-defined for matrix elements corresponding to occupied (i) – unoccupied (a) pairs, $f_i > f_a$. Only these occupied–unoccupied pairs are needed to construct the observables of interest.

The probability that a hole (electron) has been generated at time t in state i (a) is

$$P_i^{\mathrm{h}}(t) = \sum_a^{f_i>f_a} \frac{1}{2}\left[q_{ia}^2(t) + p_{ia}^2(t)\right] \tag{S12}$$

$$P_a^{\mathrm{e}}(t) = \sum_i^{f_i>f_a} \frac{1}{2}\left[q_{ia}^2(t) + p_{ia}^2(t)\right]. \tag{S13}$$

The sum of generated carriers is the same for both types

$$N_{\mathrm{carriers}}(t) = \sum_i P_i^{\mathrm{h}}(t) = \sum_a P_a^{\mathrm{e}}(t). \tag{S14}$$

These probabilities are alternatively expressed as spatial probability densities (note that we drop the explicit t dependence in q and p for brevity)

$$P_{\mathrm{h}}(\boldsymbol{r},t) = \frac{1}{2}\sum_{aii'}^{f_i>f_a,f_{i'}>f_a} (q_{ia}q_{i'a} + p_{i'a}p_{ia})\psi_i^{(0)}(\boldsymbol{r})\psi_{i'}^{(0)}(\boldsymbol{r}) \tag{S15}$$

$$P_{\mathrm{e}}(\boldsymbol{r},t) = \frac{1}{2}\sum_{iaa'}^{f_i>f_a,f_i>f_{a'}} (q_{ia}q_{ia'} + p_{ia}p_{ia'})\psi_a^{(0)}(\boldsymbol{r})\psi_{a'}^{(0)}(\boldsymbol{r}). \tag{S16}$$

Note that integrating Eq. S15 and Eq. S16 over the entire space yields the number density of carriers $\int \mathrm{d}\boldsymbol{r}P^{\mathrm{e/h}}(\boldsymbol{r},t) = N_{\mathrm{carriers}}(t)$. Further, we construct spatio-energetic probability density contributions

$$P_{\mathrm{h}}(\varepsilon,\boldsymbol{r},t) = \frac{1}{2}\sum_{aii'}^{f_i>f_a,f_{i'}>f_a} (q_{ia}q_{i'a} + p_{i'a}p_{ia})\psi_i^{(0)}(\boldsymbol{r})\psi_{i'}^{(0)}(\boldsymbol{r})\delta(\varepsilon-\varepsilon_i) \tag{S17}$$

$$P_{\mathrm{e}}(\varepsilon,\boldsymbol{r},t) = \frac{1}{2}\sum_{iaa'}^{f_i>f_a,f_i>f_{a'}} (q_{ia}q_{ia'} + p_{ia}p_{ia'})\psi_a^{(0)}(\boldsymbol{r})\psi_{a'}^{(0)}(\boldsymbol{r})\delta(\varepsilon-\varepsilon_a). \tag{S18}$$

The δ-functions in energy are in practice approximated by a Gaussian $(2\pi\sigma^2)^{-1/2}\exp(-\varepsilon^2/2\sigma^2)$ with width $\sigma = 0.07\,\mathrm{eV}$. There is no unique definition for the simultaneous decomposition in time and energy but we obtain consistent results (Fig. S13) with different variants of the former expressions. Note that in contrast to Ref. 5 we include the summation of non-degenerate ii' and aa' which has significant implications in the NP+molecule system (Fig. S13).

In this work, we calculate the fraction of generated carriers in particular regions, i.e., the Voronoi region of the molecule or the Voronoi region of a particular atomic site

$$P^{\mathrm{h,region}}(t) = \int_{\mathrm{region}} \mathrm{d}\boldsymbol{r} P_{\mathrm{h}}(\boldsymbol{r},t)/N_{\mathrm{carriers}}(t) \tag{S19}$$

$$P^{\mathrm{e,region}}(t) = \int_{\mathrm{region}} \mathrm{d}\boldsymbol{r} P_{\mathrm{e}}(\boldsymbol{r},t)/N_{\mathrm{carriers}}(t). \tag{S20}$$

Similarly, we calculate the energetic distribution in a particular region

$$P^{\mathrm{h,region}}(\varepsilon,t) = \int_{\mathrm{region}} \mathrm{d}\boldsymbol{r} P_{\mathrm{h}}(\varepsilon,\boldsymbol{r},t) \tag{S21}$$

$$P^{\mathrm{e,region}}(\varepsilon,t) = \int_{\mathrm{region}} \mathrm{d}\boldsymbol{r} P_{\mathrm{e}}(\varepsilon,\boldsymbol{r},t). \tag{S22}$$

Supplementary Note S4: Computational details

The VASP[7–9] suite was used for all structure relaxations and total energy calculations. Ground state energies were computed using a plane-wave basis set, the projector augmented wave (PAW)[10,11] method, and the vdW-df-cx[12–15] exchange correlation (XC)-functional. The plane wave cutoff 500 eV was used. We used a Gaussian occupation number smearing scheme with the parameter 0.1 eV.

Structure relaxations were performed using the conjugate gradient relaxation method implemented in VASP. Relaxation was stopped when the maximal force on any atom fell below $0.015\,\mathrm{eV\,Å^{-1}}$. Relaxations were performed for each NP separately to obtain relaxed bare NP structures. Additionally for each NP and each adsorption site the NP+molecule system was relaxed, with all atoms allowed to move.

The open-source GPAW[16,17] code package was used for all calculations of plasmonic response and carrier generation. Kohn-Sham DFT (KS-DFT) ground state calculations were performed within the PAW[10] formalism using linear combination of atomic orbitals (LCAO) basis sets[18]; the double-ζ polarized (dzp) basis set was used for C and O, and the *pvalence*[19] basis set, which is optimized to represent bound unoccupied states, for Ag, Au and Cu. The Gritsenko-van Leeuwen-van Lenthe-Baerends-solid-correlation (GLLB-sc)[20,21] XC functional was used. A simulation cell of $32\,\mathrm{Å} \times 32\,\mathrm{Å} \times 38.4\,\mathrm{Å}$ was used to represent wave functions, XC, and Coulomb potentials, with a grid spacing of 0.2 Å for wave functions and 0.1 Å for potentials. The Coulomb potential was represented in numerical form on the grid, with an additional analytic moment correction[22] centered at the NP. Fermi-Dirac occupation number smearing with width 0.05 eV was used for all calculations, except for the Cu corner site for distances $\geq$2.7 Å and for Au (111) on-top distances between 3.1 and 3.7 Å. The effect of different occupation number smearing is negligible for our results (Fig. S14). The self-consistent loop was stopped when the integral of the difference between two subsequent densities was less than 1×10^{-8}. Pulay[23]-mixing was used to accelerate the ground state convergence.

The LCAO-RT-TDDFT implementation[19] in GPAW was used for the RT-TDDFT calculations. A δ-kick strength of $K_z = 10^{-5}$ in atomic units was used. The time propagation was done in steps of 10 as for a total length of 30 fs using the adiabatic GLLB-sc kernel. We computed carrier generation for an external electric field corresponding to an ultra-short Gaussian laser pulse

$$\mathcal{E}_z(t) = \mathcal{E}_0 \cos(\omega_0 t)\exp(-(t-t_0)^2/\tau_0^2) \tag{S23}$$

of frequency ω, strength $\mathcal{E}_0 = 51\,\mathrm{\mu V\,Å^{-1}}$, peak time $t_0 = 10\,\mathrm{fs}$, and duration $\tau_0 = 3.0\,\mathrm{fs}$.

We computed the total density of states (DOS) as

$$\sum_k \delta(\varepsilon - \varepsilon_k) \tag{S24}$$

and the molecular projected DOS (PDOS) as

$$\sum_k \delta(\varepsilon - \varepsilon_k) \int_{\text{molecule}} \left|\phi_k^{(0)}(\boldsymbol{r})\right|^2 \mathrm{d}\boldsymbol{r}, \tag{S25}$$

where ε_k and $\phi_k^{(0)}(\boldsymbol{r})$ are the KS eigenvalues and wave functions. For visualization, the δ-functions in energy were replaced by a Gaussian $(2\pi\sigma^2)^{-1/2}\exp(-\varepsilon^2/2\sigma^2)$ with width $\sigma = 0.05\,\text{eV}$.

Supplementary References

[1] Marek Gajdo, Andreas Eichler, and Jürgen Hafner. CO adsorption on close-packed transition and noble metal surfaces: Trends from *ab initio* calculations. *Journal of Physics: Condensed Matter*, 16(8):1141–1164, 2004. doi: 10.1088/0953-8984/16/8/001.

[2] Edward J. Moler, Scot A. Kellar, W. R. A. Huff, Zahid Hussain, Yufeng Chen, and David A. Shirley. Spatial structure determination of $(\sqrt{3}\times\sqrt{3})$r30° and (1.5×1.5)r18° co or cu(111) using angle-resolved photoemission extended fine structure. *Physical Review B*, 54(15):10862–10868, 1996. doi: 10.1103/PhysRevB.54.10862.

[3] C. J. Hirschmugl, G. P. Williams, F. M. Hoffmann, and Y. J. Chabal. Adsorbate-substrate resonant interactions observed for Co on Cu(100) and (111) in the far-ir using synchrotron radiation. *Journal of Electron Spectroscopy and Related Phenomena*, 54-55:109–114, 1990. ISSN 0368-2048. doi: 10.1016/0368-2048(90)80203-M.

[4] R. Raval, S. F. Parker, M. E. Pemble, P. Hollins, J. Pritchard, and M. A. Chesters. FT-rairs, eels and leed studies of the adsorption of carbon monoxide on Cu(111). *Surface Science*, 203(3): 353–377, 1988. ISSN 0039-6028. doi: 10.1016/0039-6028(88)90088-X.

[5] Tuomas P. Rossi, Paul Erhart, and Mikael Kuisma. Hot-Carrier Generation in Plasmonic Nanoparticles: The Importance of Atomic Structure. *ACS Nano*, 14(8):9963–9971, 2020. doi: 10.1021/acsnano.0c03004.

[6] K. Yabana and G. F. Bertsch. Time-dependent local-density approximation in real time. *Physical Review B*, 54(7):4484–4487, 1996. doi: 10.1103/PhysRevB.54.4484.

[7] G. Kresse and J. Hafner. Ab initio molecular dynamics for liquid metals. *Physical Review B*, 47 (1):558–561, 1993. doi: 10.1103/PhysRevB.47.558.

[8] G. Kresse and J. Furthmüller. Efficient iterative schemes for ab initio total-energy calculations using a plane-wave basis set. *Physical Review B*, 54(16):11169–11186, 1996. doi: 10.1103/PhysRevB.54.11169.

[9] G. Kresse and J. Furthmüller. Efficiency of ab-initio total energy calculations for metals and semiconductors using a plane-wave basis set. *Computational Materials Science*, 6(1):15–50, 1996. doi: 10.1016/0927-0256(96)00008-0.

[10] P. E. Blöchl. Projector augmented-wave method. *Physical Review B*, 50(24):17953–17979, 1994. doi: 10.1103/PhysRevB.50.17953.

[11] G. Kresse and D. Joubert. From ultrasoft pseudopotentials to the projector augmented-wave method. *Physical Review B*, 59(3):1758–1775, 1999. doi: 10.1103/PhysRevB.59.1758.

[12] M. Dion, H. Rydberg, E. Schröder, D. C. Langreth, and B. I. Lundqvist. Van der Waals Density Functional for General Geometries. *Physical Review Letters*, 92(24):246401, 2004. doi: 10.1103/PhysRevLett.92.246401.

[13] Kristian Berland and Per Hyldgaard. Exchange functional that tests the robustness of the plasmon description of the van der Waals density functional. *Physical Review B*, 89(3):035412, 2014. doi: 10.1103/PhysRevB.89.035412.

[14] Jiří Klimeš, David R. Bowler, and Angelos Michaelides. Chemical accuracy for the van der Waals density functional. *Journal of Physics: Condensed Matter*, 22(2):022201, 2009. doi: 10.1088/0953-8984/22/2/022201.

[15] Guillermo Román-Pérez and José M. Soler. Efficient Implementation of a van der Waals Density Functional: Application to Double-Wall Carbon Nanotubes. *Physical Review Letters*, 103(9):096102, 2009. doi: 10.1103/PhysRevLett.103.096102.

[16] J. J. Mortensen, L. B. Hansen, and K. W. Jacobsen. Real-space grid implementation of the projector augmented wave method. *Physical Review B*, 71(3):035109, 2005. doi: 10.1103/PhysRevB.71.035109.

[17] J Enkovaara, C Rostgaard, J J Mortensen, J Chen, M Dułak, L Ferrighi, J Gavnholt, C Glinsvad, V Haikola, H A Hansen, H H Kristoffersen, M Kuisma, A H Larsen, L Lehtovaara, M Ljungberg, O Lopez-Acevedo, P G Moses, J Ojanen, T Olsen, V Petzold, N A Romero, J Stausholm-Møller, M Strange, G A Tritsaris, M Vanin, M Walter, B Hammer, H Häkkinen, G K H Madsen, R M Nieminen, J K Nørskov, M Puska, T T Rantala, J Schiøtz, K S Thygesen, and K W Jacobsen. Electronic structure calculations with GPAW: A real-space implementation of the projector augmented-wave method. *Journal of Physics: Condensed Matter*, 22(25):253202, 2010. doi: 10.1088/0953-8984/22/25/253202.

[18] A. H. Larsen, M. Vanin, J. J. Mortensen, K. S. Thygesen, and K. W. Jacobsen. Localized atomic basis set in the projector augmented wave method. *Physical Review B*, 80(19):195112, 2009. doi: 10.1103/PhysRevB.80.195112.

[19] M. Kuisma, A. Sakko, T. P. Rossi, A. H. Larsen, J. Enkovaara, L. Lehtovaara, and T. T. Rantala. Localized surface plasmon resonance in silver nanoparticles: Atomistic first-principles time-dependent density-functional theory calculations. *Physical Review B*, 91(11):115431, 2015. doi: 10.1103/PhysRevB.91.115431.

[20] Oleg Gritsenko, Robert van Leeuwen, Erik van Lenthe, and Evert Jan Baerends. Self-consistent approximation to the Kohn-Sham exchange potential. *Physical Review A*, 51(3):1944, 1995. doi: 10.1103/PhysRevA.51.1944.

[21] M. Kuisma, J. Ojanen, J. Enkovaara, and T. T. Rantala. Kohn-Sham potential with discontinuity for band gap materials. *Physical Review B*, 82(11):115106, 2010. doi: 10.1103/PhysRevB.82.115106.

[22] A Castro, A Rubio, and M J Stott. Solution of Poisson's equation for finite systems using plane-wave methods. *Canadian Journal of Physics*, 81(10):1151–1164, 2003. doi: 10.1139/p03-078.

[23] Péter Pulay. Convergence acceleration of iterative sequences. the case of scf iteration. *Chemical Physics Letters*, 73(2):393–398, 1980. doi: 10.1016/0009-2614(80)80396-4.